Readout Techniques for High-Q Micromachined Vibratory Rate Gyroscopes

Chinwuba David Ezekwe

Electrical Engineering and Computer Sciences
University of California at Berkeley

Technical Report No. UCB/EECS-2007-176
http://www.eecs.berkeley.edu/Pubs/TechRpts/2007/EECS-2007-176.html

December 21, 2007

Copyright © 2007, by the author(s).
All rights reserved.

Permission to make digital or hard copies of all or part of this work for personal or classroom use is granted without fee provided that copies are not made or distributed for profit or commercial advantage and that copies bear this notice and the full citation on the first page. To copy otherwise, to republish, to post on servers or to redistribute to lists, requires prior specific permission.

Readout Techniques for High-Q Micromachined Vibratory Rate Gyroscopes

by

Chinwuba David Ezekwe

B.S. (University of California, Berkeley) 2000

A dissertation submitted in partial satisfaction
of the requirements for the degree of

Doctor of Philosophy

in

Engineering - Electrical Engineering and Computer Sciences

in the

GRADUATE DIVISION

of the

UNIVERSITY OF CALIFORNIA, BERKELEY

Committee in charge:

Professor Bernhard E. Boser, Chair
Professor Kristofer S. J. Pister
Professor Roberto Horowitz

Fall 2007

The dissertation of Chinwuba David Ezekwe is approved.

Chair Date

Date

Date

University of California, Berkeley

Fall 2007

Readout Techniques for High-Q Micromachined Vibratory Rate Gyroscopes

Copyright © 2007

by

Chinwuba David Ezekwe

Abstract

Readout Techniques for High-Q Micromachined Vibratory Rate Gyroscopes

by

Chinwuba David Ezekwe

Doctor of Philosophy in Engineering - Electrical Engineering and Computer Sciences

University of California, Berkeley

Professor Bernhard E. Boser, Chair

Inexpensive MEMS gyroscopes are enabling a wide range of automotive and consumer applications. Examples include image stabilization in cameras, game consoles, and improving vehicle handling on challenging terrain. Many of these applications impose very stringent requirements on power dissipation. For continued expansion into new applications it is imperative to reduce power consumption of present devices by an order-of-magnitude.

Gyroscopes infer angular rate from measuring the Coriolis force exerted on a vibrating or rotating mass. For typical designs and inputs, this signal is extremely small, requiring ultralow noise pickup electronic circuits. This low noise requirement directly translates into excessive power dissipation.

This work describes a solution that combines a new low-power electronic readout circuit with mechanical signal amplification using a technique called mode-matching. The electronic circuit continuously senses the resonance frequency of the mechanical sense element and electrically tunes it to maximize the output signal. A new and robust feedback controller is used to accurately control the scaling factor and bandwidth of the gyroscope while at the same time guaranteeing stability in the presence of undesired parasitic resonances.

The circuit has been fabricated in a 0.35μm CMOS process and consumes less than 1mW. The spot noise is $0.004\,^\circ/\mathrm{s}/\sqrt{\mathrm{Hz}}$.

Professor Bernhard E. Boser
Dissertation Committee Chair

To my late father.

Contents

Contents ii

Acknowledgements iv

1 Introduction 1

2 Power-Efficient Coriolis Sensing 4

2.1 Review of Vibratory Gyroscopes 4

2.2 Electronic Interface 5

2.3 Readout Interface 7

2.4 Improving Readout Interface Power Efficiency 9

2.5 Exploiting the Sense Resonance 11

3 Mode Matching 15

3.1 Estimating the Mismatch 16

3.2 Tuning Out the Mismatch 21

3.3 Closing the Tuning Loop 22

3.4 Practical Considerations 24

3.4.1 Practical Signal Synthesis, Demodulation, and Filtering 24

3.4.2 Finite Force Feedback Open-Loop Gain 27

3.4.3 Interference from Large Inertial Forces 28

3.5 Summary 30

4 Position Sensing 31

4.1 Force Feedback Loop Stability Consideration 31

4.2 Sampling and Noise Folding 32

4.3 Boxcar Sampling 35
4.4 Removing Switch kT/C Noise and Amplifier $1/f$ Noise 39
4.5 Other Practical Considerations 40
4.6 Summary 43

5 Force Feedback **45**
5.1 Mode-Matching Consideration 45
5.2 Preliminary System Architecture and Model for Stability Analysis . . 47
5.3 Accommodating Parasitic Resonances 48
5.3.1 Traditional Lead Compensation 50
5.3.2 Positive Feedback Technique 51
5.4 Positive Feedback Architecture 55
5.4.1 Setting the Open-Loop DC Gain 55
5.4.2 Accommodating Sensor Offset 58
5.4.3 System Design 60
5.5 Summary 63

6 An Experimental Readout Interface **65**
6.1 Implementation 65
6.1.1 Front-End and 3-Bit DAC 67
6.1.2 Compensator 68
6.2 Experimental Results 72
6.3 Summary 77

7 Conclusions **78**
7.1 Results 78
7.2 Future Work 79

Bibliography **80**

Acknowledgements

I would like to thank Professor Bernhard E. Boser for his continuing support, guidance and encouragement and for giving me the independence to follow my ideas wherever they led. His constant but constructive criticisms were key in the successful outcome of this study. I would like to thank Professor Kristofer S. J. Pister for his continuing support and guidance. He challenged me while I was an undergraduate, recommended me for graduate study, and steered me in the direction most suited to my strengths. I would also like to thank Professor Seth R. Sanders and Professor Steven D. Glaser for listening to my ideas and providing me with useful feedback during my qualifying examination and Professor Roberto Horowitz for reading my dissertation.

I conducted a major portion of this work at the Robert Bosch Research and Technology Center, where I had the benefit of receiving tremendous help from Christoph Lang, Vladimir P. Petkov, Johan P. Vanderhaegen, Xinyu Xing and others, and Gerhard Schneider, who provided all necessary accommodations to facilitate my work at Bosch. I extend special thanks to them all.

I thank my friends and colleagues in the Berkeley EECS department. Sarah Bergbreiter, Baris Cagdaser, Octavian Florescu, Steven M. Lanzisera, Matthew E. Last, Brian S. Leibowitz, Travis L. Massey, Ankur M. Mehta, Mike D. Scott, George W. Shaw, Karl R. Skucha, Jason T. Stauth, Subramaniam Venkatraman, David Zats and others in the department made my graduate school experience very enjoyable.

I thank Ruth Gjerde and Mary K. Byrnes in the Graduate Student Affairs offices for their eagerness to extend help on numerous occasions.

I am very grateful to my wife for her love, support, encouragement, and understanding. Her sacrifice gave me the freedom to concentrate on, and complete, this study. I am forever indebted to my late father, my mother, and my sister for their many sacrifices. I thank my daughter for being patient with me while I was writing this dissertation. I thank my and my wife's extended family for their support.

This research was funded by Robert BOSCH LLC.

Chapter 1

Introduction

Motion sensing is finding increasing application in various equipments such as cameras that compensate for image blur caused by camera shake and vehicles that prevent loss of control on sudden swerving by the driver. In the vehicle, as in the camera, compensation for the undesired movement is enabled by a micromachined angular rate sensor, a complex system consisting of a mechanical element that senses the physical motion and electronic circuits that read out the motion.

While the application domain of micromachined angular rate sensors, or gyroscopes as they are commonly called, has continued to expand, for example into inertial navigation and virtual reality, the power dissipation of the electronic circuits, failing to keep pace with general improvements expected with each electronic device generation, is becoming too prohibitive for present applications and is threatening the emergence of new ones. Whether it is in the hand-held consumer electronics space where battery life is the principal consideration or in the automotive arena where the power dissipated and the consequent heat produced by the sensor cluster call for expensive packaging and constrain the expansion of sensing capability, the power dissipation of current state-of-the-art micromachined gyroscopes is quickly becoming a limiting factor.

This work focuses on achieving the substantial improvements in power efficiency essential for the continued expansion of micromachined gyroscopes into new application. Proposed in this dissertation is a readout architecture which, with only a modest

increase in the complexity of the electronic circuits, exploits opportunities inherent in the sensor and elsewhere to reduce power dissipation by orders-of-magnitude without compromising any aspect of sensor performance.

After providing a brief review of vibratory gyroscopes, the most prevalent kind of micromachined angular rate sensors, the next chapter begins consideration of the electronics with particular emphasis on the readout interface. The chapter proposes matching the drive and sense resonance modes of the sense element as a means to substantially reduce power dissipation and further proposes force feedback as a means to overcome the difficulties that have until now prevented the full exploitation of mode-matching.

Full exploitation of mode-matching requires a level of frequency matching beyond manufacturing limits. Chapter 3 introduces a resonance frequency calibration technique to overcome the limits imposed by manufacturing tolerances. Unlike previously reported schemes, this technique continuously and automatically tunes the resonance frequencies while the sense element is an active force feedback loop, avoiding costly in-factory calibration.

Feedback generally relaxes the requirements of the blocks in the forward path. Focusing on the position sense front-end, the block that dominates active power dissipation, Chapter 4 proposes a front-end architecture that exploits the presence of the front-end in the forward path of the force feedback to achieve additional reductions in power dissipation.

Designing the force feedback loop in a way that is compatible with other aspects of the proposed architecture is essential for the whole system to work. Chapter 5 focuses on the design of the force feedback loop with particular emphasis on preserving analog simplicity while ensuring that the loop is compatible with the mode-matching algorithm and the highly underdamped resonances of a vacuum packaged sensor.

The techniques discussed in Chapters 3, 4, and 5 are applied in Chapter 6 towards the implementation of an experimental readout interface in a 0.35μm CMOS process. The interface consumes less than 1mW and achieves a spot noise of $0.004\,^\circ/\mathrm{s}/\sqrt{\mathrm{Hz}}$ over a 50Hz band.

The last chapter, Chapter 7, summarizes the main results of this work and concludes with suggestions for future research.

Chapter 2

Power-Efficient Coriolis Sensing

After a brief review of the basic operating principle of vibratory gyroscopes, this chapter focuses on the electronic interface in search of opportunities to lower its power dissipation. The chapter proposes mode-matching as a means to reduce power dissipation by orders of magnitude from the levels set by state-of-the-art interfaces and presents the basic elements of a readout architecture that enables the effective exploitation of the proposed means.

2.1 Review of Vibratory Gyroscopes

Figure 2.1 illustrates the basic operating principle of vibratory gyroscopes. A proof mass suspended by springs to a frame is maintained in a steady-state oscillatory motion along the drive axis. Rotation of the frame in the plane formed by the drive and sense axes produces, along the sense axis, a Coriolis acceleration that is proportional to the product of the drive velocity and the angular rate. If we express the drive oscillation as $x_d = x_{d0}\cos(\omega_d t)$ where x_{d0} and ω_d are respectively the amplitude and angular frequency of the drive oscillation, then the Coriolis acceleration

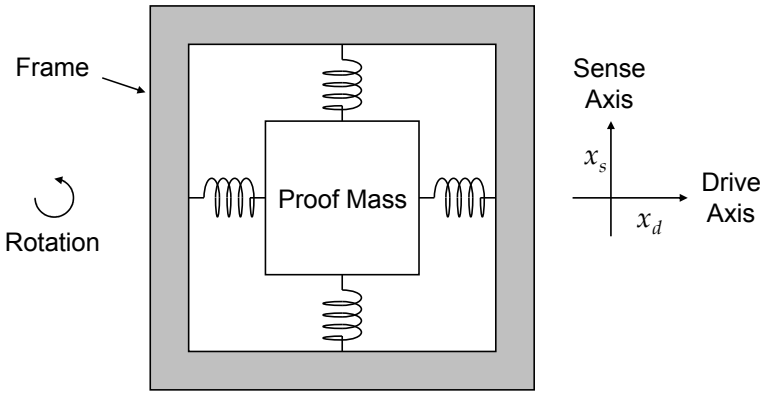

Figure 2.1. Vibratory gyroscope operating principle.

due to an angular rate Ω is

$$\begin{aligned} a_c &= 2\,\Omega\,\dot{x}_d \\ &= -\underbrace{2\,\Omega\,\omega_d\,x_{d0}}_{a_{c0}}\sin(\omega_d t) \end{aligned} \tag{2.1}$$

where a_{c0} is the amplitude of the oscillatory Coriolis acceleration. The angular rate Ω is inferred from measuring the Coriolis acceleration a_c.

To first order, each axis of a vibratory gyroscope is a second-order system. Vacuum packaging results in highly under-damped resonance modes. The resonance mode along the drive axis is referred to as the drive mode and the one along the sense axis is referred to as the sense mode. The two resonance frequencies are usually mismatched intentionally or due to process variations. Figure 2.2 shows a schematic illustration of the frequency response along the drive and sense axes. The drive oscillation normally occurs at the drive resonance frequency to benefit from the amplification by the quality factor of the drive mode. Consequently, the Coriolis acceleration is also centered at the drive resonance.

2.2 Electronic Interface

Figure 2.3 shows a simple generalized model of a gyroscope with the electronic interface necessary to produce the final output. An oscillator establishes the above mentioned drive oscillation at the drive resonance frequency, and the Coriolis readout

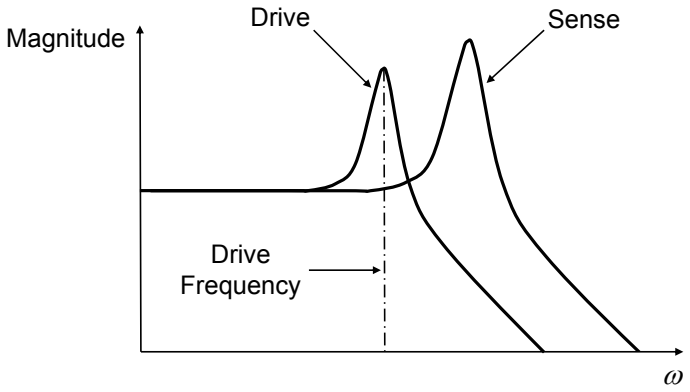

Figure 2.2. Vibratory gyroscope frequency characteristics.

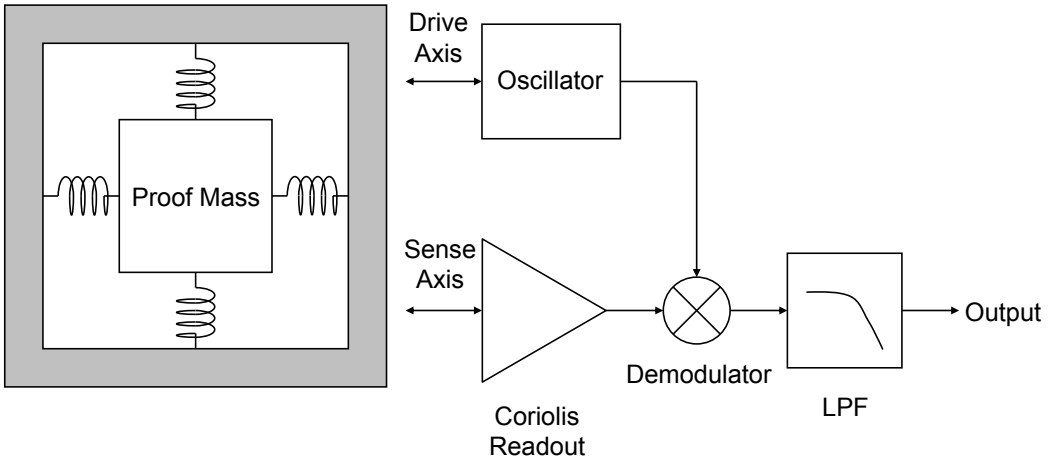

Figure 2.3. Simplified model of gyroscope with the necessary electronic interface.

interface detects and amplifies the Coriolis acceleration. A demodulator demodulates the angular rate signal from the Coriolis acceleration, and a low-pass filter removes, from the final output, artifacts of the demodulation and other unwanted signals outside the desired frequency band.

The high quality factors achievable with vacuum packaging greatly relax the oscillator power requirements. The demodulator and low-pass filter contribute marginally to the overall interface power dissipation since they handle already amplified signals and thus are not noise limited. This leaves the readout interface which detects Coriolis accelerations with extremely high precision as the dominant source of power dissipation. Many applications require a digital output resulting in additional power dissipation in the analog-to-digital conversion. The readout interface, therefore, holds the key to substantial reductions in the overall electronic interface power dissipation.

2.3 Readout Interface

The readout interface senses the Coriolis acceleration indirectly by detecting the motion the Coriolis acceleration induces on the proof mass along the sense axis. The induced motion is oscillatory and is of the form $x_s = x_{s0}\sin(\omega_d t + \phi_s)$ where x_{s0} is the amplitude of the motion and ϕ_s is the phase lag of the sense axis response at the drive frequency. The motion is detected by measuring the capacitance between the proof mass and fixed electrodes. The capacitance varies with, and is thus a good indicator of, displacement. Capacitive sensing is attractive for low cost inertial sensors because it is compatible with most fabrication processes and the capacitive interface can be easily used for force actuation. The capacitance is normally implemented with transverse comb fingers for maximum displacement-to-capacitance sensitivity which is advantageous for maximizing the overall sensitivity of the sense element.

Figure 2.4 illustrates the most basic readout interface consisting of the sense element and a position sense front-end amplifier. A simple suspension with four beams that are compliant in both the drive and sense directions is shown; in practice, more elaborate solutions that enable the independent optimization of the drive and sense modes are preferred [1, 2]. The front-end amplifier converts the differential capaci-

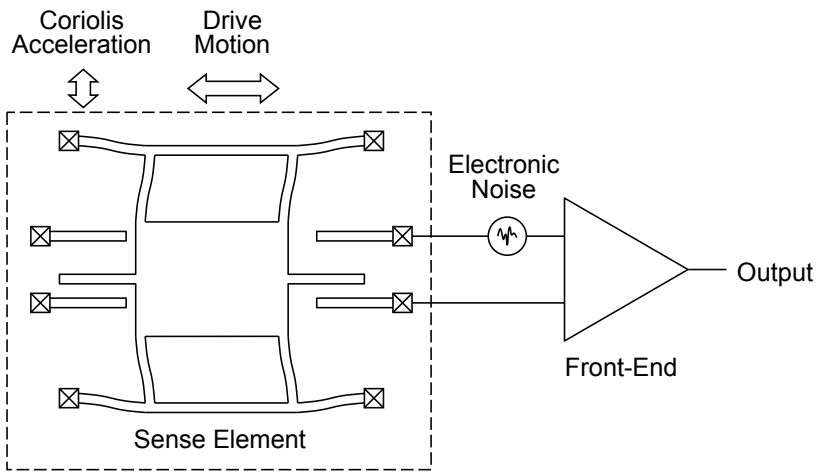

Figure 2.4. Basic Coriolis readout interface (drive details omitted).

tance between the proof mass and the fixed electrodes into voltage or current. Unfortunately, the amplifier's output will, invariably, be corrupted by electronic noise which we model by an equivalent source in series with the input of the amplifier. This noise limits the displacement resolution of the front-end and directly impacts the power dissipation of the overall interface.

A key performance metric for any sensor is the minimum detectable signal. For vibratory gyroscopes, the fundamental limit is set by (1) the Brownian motion of the gas surrounding the proof mass and (2) the thermal noise of the circuit elements comprising the readout interface. For maximum performance (resolution), the Brownian motion should dominate the system noise floor to preserve the intrinsic performance of the sense element, but often and especially in systems that are operated in vacuum, circuit noise dominates over Brownian noise. In such cases, reducing the minimum detectable signal within a given bandwidth by a factor of two requires a proportional reduction in the standard deviation of the circuit noise within the same bandwidth which, in turn, requires a four-fold increase in device currents. Improving the angular rate resolution without the associated increase in power dissipation is thus a major challenge.

Since, due to manufacturing tolerances, the drive and sense springs are imperfectly orthogonal, some of the drive oscillation leaks directly into the sense axis, resulting in large undesired sense axis oscillatory motion that is in quadrature with the desired

Coriolis acceleration induced motion. The demodulation signal from the oscillator circuit normally has substantial phase noise which the so called quadrature error can mix down reciprocally, raising the overall interface noise floor beyond that set by the front-end. Fortunately, most but not all of the quadrature error can be nulled using special quadrature nulling electrodes [3]. The residual error can be rejected during the demodulation process by using an appropriately phased demodulation signal since the error is in quadrature with the desired signal. Achieving a high degree of rejection requires a well defined phase relationship between the quadrature error and the drive oscillation from which the demodulation signal is normally derived. Ensuring that the phase relationship is well defined is the second significant challenge for the readout interface.

There is also the Coriolis offset which comes from leakage of the drive force into the sense axis due to misalignment of the drive combs. This error is minimized by vacuum packaging since the increased quality factors enable the use of smaller drive forces which result in smaller forces feeding through to the sense axis [4].

Other challenges include obtaining a wide enough signal bandwidth and ensuring that the overall gain (scale factor) is stable over fabrication tolerances and ambient variations. A wide bandwidth is necessary especially in control applications such as vehicle stability control where sensors with minimum phase lag are required.

2.4 Improving Readout Interface Power Efficiency

In a vibratory gyroscope, rotation is converted to Coriolis acceleration that is detected by measuring the consequent motion of the proof mass. A "rate grade" resolution of $0.1\,^\circ/\mathrm{s}/\sqrt{\mathrm{Hz}}$ translates into a displacement resolution on the order of $100\,\mathrm{fm}/\sqrt{\mathrm{Hz}}$ in typical gyroscope designs. Current state-of-the art interfaces resolve $60\,\mathrm{fm}/\sqrt{\mathrm{Hz}}$ while dissipating 30 mW [2]. Applications such as image stabilization in cameras and vehicle stability control require an order of magnitude better angular rate resolution for similar or lower power dissipation. Unfortunately, power dissipation in a noise limited readout interface is, to first order, inversely proportional to the square of the displacement resolution. Thus, while $0.01\,^\circ/\mathrm{s}/\sqrt{\mathrm{Hz}}$ can be achieved

through traditional means by simply resolving $10\,\mathrm{fm}/\sqrt{\mathrm{Hz}}$, the 1 W of power required makes such a noise floor impractical in the target applications. Essentially, the readout interface power efficiency must be improved to enable the use of high-resolution angular rate sensors in power constrained applications. Increasing the signal-to-noise ratio (SNR) passively requires increasing the sense element's angular rate-to-sense motion sensitivity ($\Delta x_{s0}/\Delta\Omega$) so that the same angular rate produces a larger sense motion amplitude.

The angular rate-to-sense motion sensitivity can be expressed as the product of two factors:

$$\frac{\Delta x_{s0}}{\Delta\Omega} = \left(\frac{\Delta a_{c0}}{\Delta\Omega}\right)\left(\frac{\Delta x_{s0}}{\Delta a_{c0}}\right). \tag{2.2}$$

The first factor is the angular rate-to-Coriolis acceleration sensitivity which indicates the amplitude of the Coriolis acceleration produced by a given angular rate. This factor is normally maximized by a large drive oscillation amplitude. The second factor is the Coriolis acceleration-to-sense motion sensitivity which indicates the sense motion amplitude resulting from a given Coriolis acceleration amplitude. The drive and sense resonance frequencies are normally mismatched either by design or due to fabrication tolerances and ambient variations. However, if they were perfectly matched, the Coriolis acceleration would be centered at the sense mode frequency, and because of the consequent amplification by the sense mode quality factor, the same Coriolis acceleration, and consequently the same angular rate, would produce a much larger sense motion [5]. Continuing with the previous example and assuming a ten fold increase in Coriolis acceleration-to-sense motion sensitivity, an angular rate resolution of $0.01\,^\circ/\mathrm{s}/\sqrt{\mathrm{Hz}}$ would require a displacement resolution on the order of $100\,\mathrm{fm}/\sqrt{\mathrm{Hz}}$ rather than the more stringent $10\,\mathrm{fm}/\sqrt{\mathrm{Hz}}$, which translates into two orders of magnitude power dissipation reduction over the original example.

Based on the foregoing discussion, we propose to exploit the free mechanical amplification provided by the sense resonance to greatly relax the noise requirements, and therefore substantially reduce the power dissipation, of the readout interface.

2.5 Exploiting the Sense Resonance

Matching the drive and sense modes, or mode-matching as it is normally called, increases sense displacements by the sense mode quality factor and thereby relaxes the noise requirements of the front-end, but also brings several problems chief among which are an extremely narrow sense bandwidth due to the high quality factor, and increased gain variation and phase uncertainty due to fabrication tolerances and ambient variations. The bandwidth is given by

$$f_{BW} = \frac{f_s}{2\,Q_s} \tag{2.3}$$

where f_s and Q_s are the frequency and quality factor of the sense resonance. With mode-matching, the frequency of the sense resonance is equal to that of the drive (within engineering tolerance). The drive frequency and sense mode quality factor, typically on the order of 15 kHz and 1000 respectively, result in bandwidths on the order of 7.5 Hz which is in stark contrast to the 50 Hz required by automotive and consumer applications. The 7.5 Hz 3-dB bandwidth is moreover poorly controlled due to the normally substantial variation of the quality factor with the ambient. The variation of quality also results in gain variation. Figure 2.5 illustrates this problem. Also, the invariably limited accuracy and bandwidth of any practical mode-matching scheme will result in a small residual frequency mismatch. Especially considering the process and ambient variations of the residual mismatch, the very abrupt phase change near the sense resonance results in substantial phase uncertainty which exacerbates the task of rejecting quadrature error. Figure 2.6 illustrates this problem. Due to these difficulties, many gyroscope implementations avoid mode-matching and instead operate away from the sense resonance, obtaining a larger bandwidth and better defined gain and phase at the expense of sensitivity [6, 4]. A practical readout interface exploiting the sense resonance must overcome the problems arising from mode-matching in a way that neither interferes with gyroscope performance nor negates the power advantage derived from mode-matching.

Feedback is widely used in electronics to obtain precise characteristics, for example precise gains, from imprecise elements. It has been used in sensors to improve bandwidth, dynamic range, linearity, and drift [7, 8]. Especially in high-Q vibratory gyroscopes with matched modes, feedback is imperative to ensure proper operation.

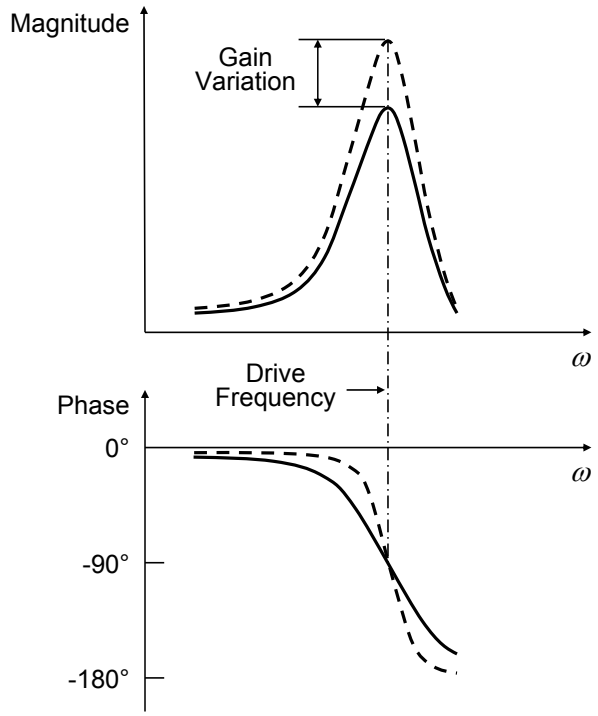

Figure 2.5. Gain (scale factor) variation with quality factor.

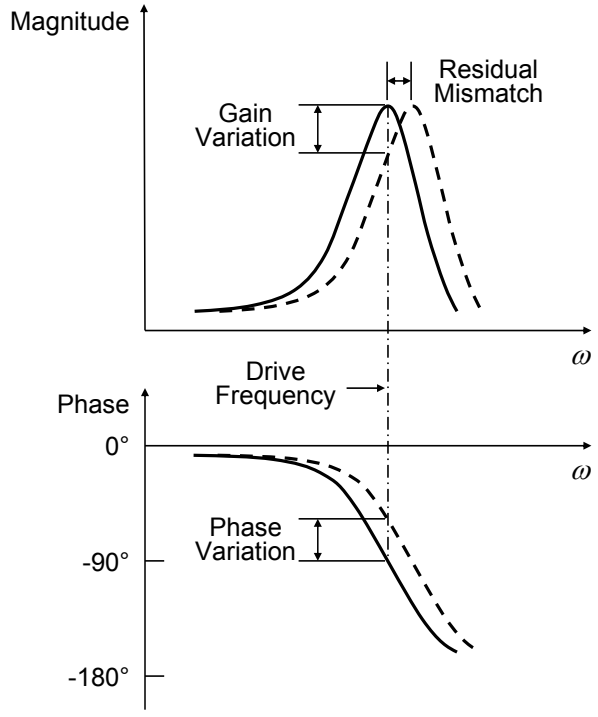

Figure 2.6. Gain and phase variation with residual mismatch.

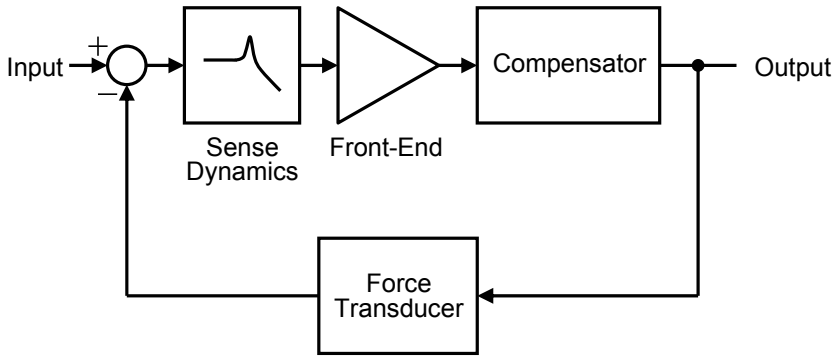

Figure 2.7. Basic force feedback loop.

Figure 2.7 shows the sense element enclosed in a force feedback loop. A compensator and a force transducer are added to the basic *open-loop* interface to form a *closed-loop* interface. Based on the motion sensed by the front-end, the compensator produces an estimate of the Coriolis force which the force transducer applies with opposite polarity on the proof mass to null the sense motion. Perfect nulling of the proof mass motion implies that the feedback force is exactly equal and opposite to the Coriolis force. While this is impossible to achieve over all frequencies in practice, adequate nulling is possible within a limited frequency band where the force feedback open-loop gain is sufficiently high. Within that frequency band, the output of the closed-loop interface is an accurate representation of the Coriolis acceleration. Figure 2.8 compares the frequency responses of the open-loop sensor and that of a closed-loop interface that has a high open-loop gain over a frequency range that extends beyond the resonance of the sense element. Electronic circuits implementing the compensator provide the necessary open-loop gain. Regardless of the variations of the sensor parameters, the closed-loop response remains flat and stable over a much wider frequency range. Thus, the traditional tradeoff of mechanical sensitivity for larger bandwidth and better defined gain and phase is unnecessary.

With force feedback, the sense resonance can be fully exploited without sacrificing other important aspects of system performance. However, successful use of the closed-loop architecture depends on key implementation details. The next three chapters further develop the architecture to address various details ignored by the simple discussion presented so far. Leaving the problem of force feedback loop design aside for a later chapter, the next chapter focuses on the problem of automatically

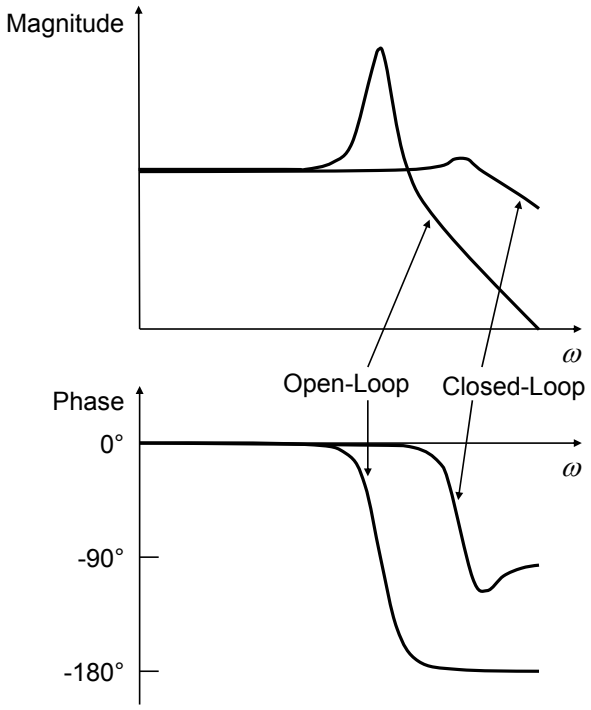

Figure 2.8. Illustrative example of sensor and closed-loop frequency responses.

matching the resonance frequencies of a gyroscope that is enclosed in a generic force feedback loop.

Chapter 3

Mode Matching

As argued in the previous chapter, matching the resonance frequencies of the drive and sense modes amplifies the sense displacement and hence has the potential to reduce the power dissipation of the readout interface. Maximizing the signal-to-noise ratio (SNR) improvement requires the frequency matching error to be less than the reciprocal of the sense mode quality factor. For example, a sense mode quality factor of 1000 requires less than 0.1% matching error. Process tolerances and ambient variations limit the minimum matching error achievable with precision manufacturing to about 2% [4], mandating resonance frequency calibration.

One way to perform the calibration is to fully characterize the dependence of frequency matching on physical parameters such as temperature and then use the data to calibrate the sense resonance frequency at runtime. Besides the added complexity of integrating additional sensors to measure the influential physical parameters, the high cost of fully characterizing the sense element at the factory puts this technique at odds with the cost constraints of MEMS gyroscope applications. The alternative and preferred way is to monitor sensor properties that vary with frequency matching. Previously proposed calibration schemes using the preferred approach determine frequency matching by monitoring sensor properties such as gain and phase lag [1, 9]. Unfortunately, those properties are not easily measurable when the sense element is part of a force feedback loop. Since force feedback is imperative to ensure proper

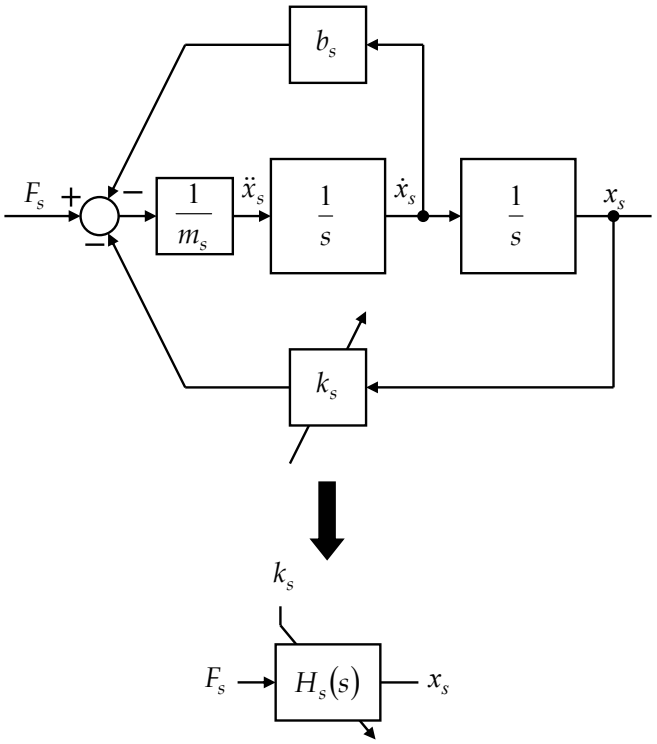

Figure 3.1. Second-order sense dynamics with variable stiffness.

operation of a mode matched gyroscope, we need to develop a way to measure the relevant sensor properties in a way that is compatible with closed-loop sensing.

3.1 Estimating the Mismatch

Figure 3.1 models the dynamics of the sense axis as a lumped spring-mass-damper system. The system has the transfer function

$$H_s(s) = \frac{1}{m_s\, s^2 + b_s\, s + k_s} \tag{3.1}$$

where m_s and b_s are respectively the mass and damping factor, and k_s is the variable stiffness which we aim to observe and ultimately control. The task of mode-matching is to force k_s to approach the optimal stiffness $k_{s,opt} = m_s\omega_d^2$. This requires the monitoring of the deviation of the actual stiffness from the optimal value.

The feedback path of a stable closed-loop system determines the closed-loop response provided that the open-loop gain is much greater than unity. We exploit this

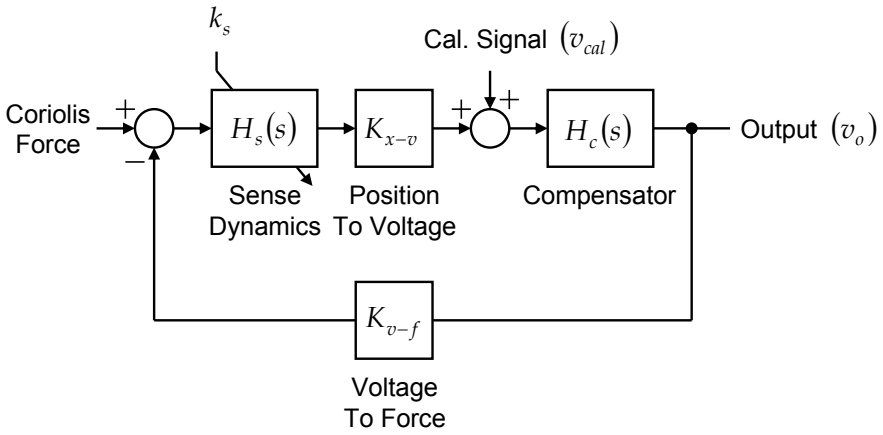

Figure 3.2. Force feedback loop with added calibration input. The sense dynamics are in the feedback path with respect to the calibration input.

property to isolate the characteristics of the sense element from the rest of the feedback loop by choosing a calibration input that places only the sense dynamics in the feedback path. Figure 3.2 shows the force feedback loop with the added calibration input. We have replaced the front-end and the force transducer by position-to-voltage gain K_{x-v} and voltage-to-force gain K_{v-f} respectively. Restating what is already well-known, the transfer function from the calibration input to the output assuming a high open-loop gain is

$$\begin{aligned} G_{cal}(s) &\approx \frac{1}{K_{v-f}\,K_{x-v}\,H_s(s)} \propto \frac{1}{H_s(s)} \\ &\approx \frac{1}{K_{v-f}\,K_{x-v}} \left(m_s\,s^2 + b_s\,s + k_s\right). \end{aligned} \tag{3.2}$$

The gain terms K_{v-f} and K_{x-v} affect only the static gain of $G_{cal}(s)$ and not the location of the complex zeros. Figure 3.3 compares the frequency responses of $H_s(s)$ and $G_{cal}(s)$. The *notch* and 90° phase *lead* of $G_{cal}(s)$ exactly mirror the *peak* and 90° phase *lag* of $H_s(s)$ at resonance making $G_{cal}(s)$ an excellent, albeit inverse, proxy for $H_s(s)$. In a sense, $G_{cal}(s)$ is preferable over $H_s(s)$ because it avoids the high-Q poles in $H_s(s)$ that severely limit the tracking bandwidth of conventional open-loop sensing based frequency calibration techniques [9].

One possible way to use the calibration input to estimate the frequency mismatch is to monitor the phase shift from the calibration input to the output using a pilot tone at the drive frequency. Unfortunately, this approach is problematic because the tone would invariably interfere with the Coriolis signal. We overcome this problem by

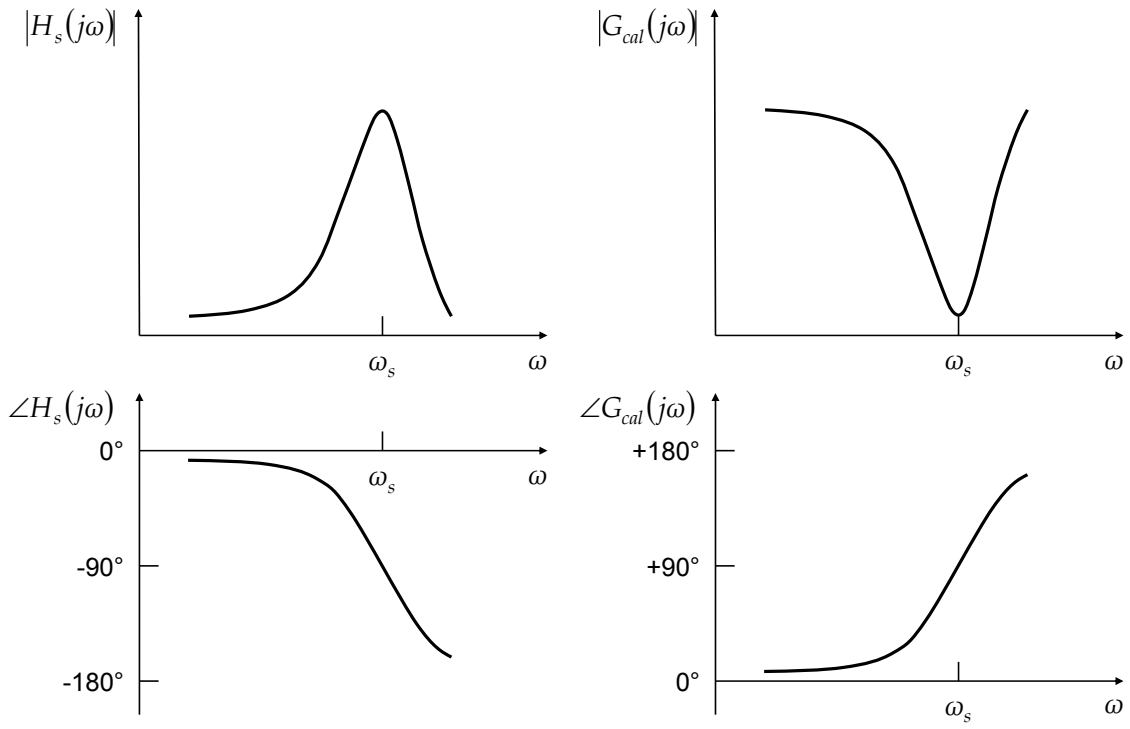

Figure 3.3. Comparison of the frequency responses of $H_s(s)$ and $G_{cal}(s)$.

using *two* pilot tones that are referenced to the drive frequency and located outside the desired signal band with one tone above and the other below the desired signal band. We adjust the tones to *equalize* their output amplitudes when the drive and sense resonance frequencies match. If after the adjustment the sense resonance frequency drifts *higher* (or *lower*) than the drive frequency, the amplitude of the higher frequency tone becomes *smaller* (or *larger*) than that of the lower frequency tone. Thus, the amplitude difference indicates the magnitude and direction of frequency mismatch. Figure 3.4 illustrates this estimation principle.

If v_1 and v_2 are the input amplitudes and ω_1 and ω_2 are the angular frequencies of the tones, then the responses at the output are

$$\begin{aligned} v_{o1} &= G_{cal}(j\omega_1)v_1 \\ &= \underbrace{\frac{v_1}{K_{v-f}\,K_{x-v}}\left(k_s - m_s\omega_1^2\right)}_{v_{o1,\mathrm{I}}} + \underbrace{j\frac{v_1}{K_{v-f}\,K_{x-v}}\,b_s\,\omega_1}_{v_{o1,\mathrm{Q}}} \end{aligned} \tag{3.3}$$

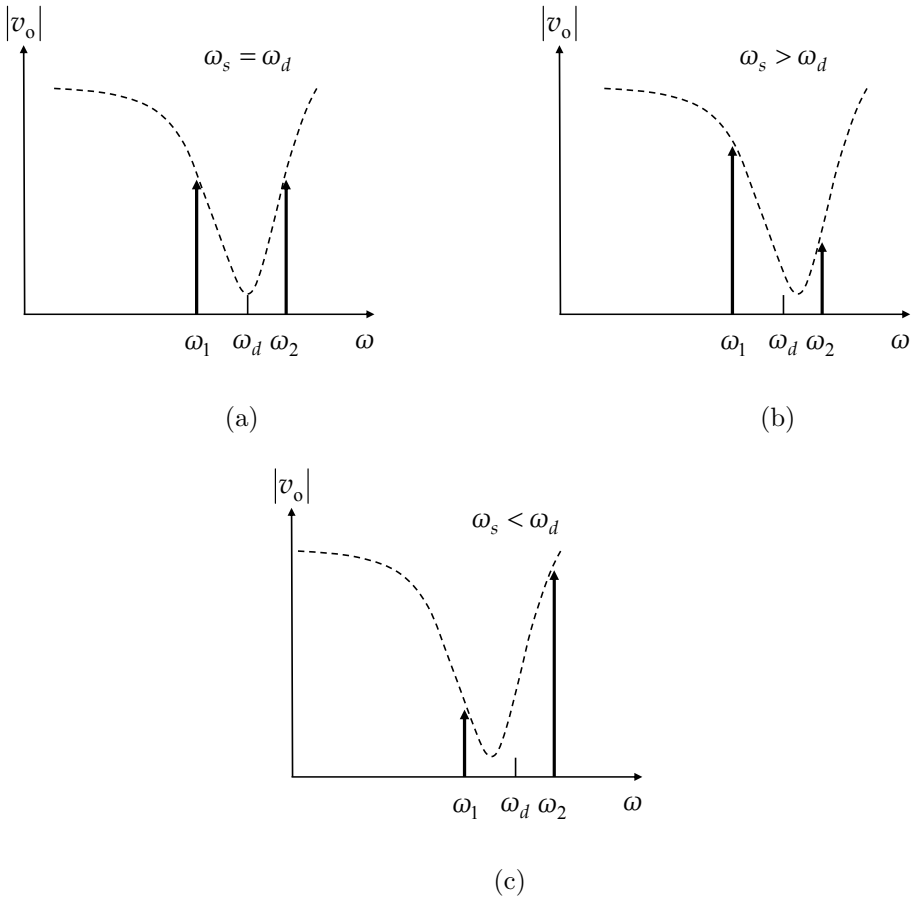

Figure 3.4. Frequency mismatch estimation principle. The dashed lines indicate $|G_{cal}(j\omega)|$. (a) The amplitudes match when the drive and sense frequencies match. The higher frequency tone becomes (b) smaller when the sense resonance frequency drifts higher, and (c) larger when the sense resonance frequency drifts lower.

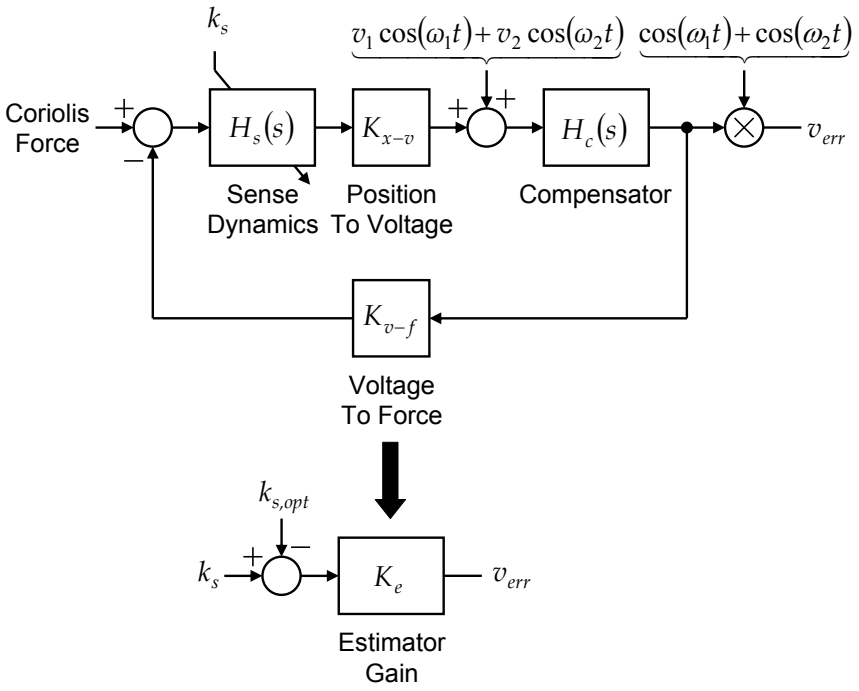

Figure 3.5. Estimator realization and linearized model.

and

$$\begin{aligned} v_{o2} &= G_{cal}(j\omega_2)v_2 \\ &= \underbrace{\frac{v_2}{K_{v-f}\,K_{x-v}}\left(k_s - m_s\omega_2^2\right)}_{v_{o2,\mathrm{I}}} + \underbrace{j\frac{v_2}{K_{v-f}\,K_{x-v}}\,b_s\,\omega_2}_{v_{o2,\mathrm{Q}}}. \end{aligned} \tag{3.4}$$

The *in-phase* terms $v_{o1,\mathrm{I}}$ and $v_{o2,\mathrm{I}}$ are useful since they are modulated by k_s. The *quadrature* terms $v_{o1,\mathrm{Q}}$ and $v_{o2,\mathrm{Q}}$ are useless and are rejected by synchronously demodulating the in-phase terms. Their rejection makes this approach insensitive to damping factor variations to first order. Another welcome feature of synchronous demodulation is that it preserves the signs of the in-phase terms. This, combined with the phase inversion beyond the sense resonance frequency, allows amplitude differencing to be realized by simply summing $v_{o1,\mathrm{I}}$ and $v_{o2,\mathrm{I}}$.

Figure 3.5 shows the very simple realization of the estimator. Signals similar to

the pilot tones are used in the demodulation. The final error signal is

$$\begin{aligned} v_{err} &= v_{o1,\mathrm{I}} + v_{o2,\mathrm{I}} \\ &= \underbrace{\frac{v_1 + v_2}{K_{v-f}\, K_{x-v}}}_{\text{estimator gain}} \left[k_s - \underbrace{m_s \left(\frac{\omega_1^2}{1 + \dfrac{v_2}{v_1}} + \frac{\omega_2^2}{1 + \dfrac{v_1}{v_2}} \right)}_{\text{reference stiffness}} \right]. \end{aligned} \tag{3.5}$$

We adjust the pilot tone parameters as previously mentioned such that the reference stiffness is equal to the optimal stiffness $k_{s,opt}$. If we fix the tone frequencies to $\omega_1 = \omega_d - \omega_{cal}$ and $\omega_2 = \omega_d + \omega_{cal}$, then the amplitudes must satisfy

$$\frac{v_2}{v_1} = \frac{2\omega_d - \omega_{cal}}{2\omega_d + \omega_{cal}}. \tag{3.6}$$

The unequal amplitudes account for the logarithmic nature of frequency behavior and the asymmetry between the low and high frequency responses of $G_{cal}(s)$. The constraint results in an error signal that is exactly proportional to the difference between the actual stiffness and the optimal stiffness, i.e. $v_{err} = K_e\,(k_s - k_{s,opt})$ where K_e is the estimator gain.

3.2 Tuning Out the Mismatch

Figure 3.6 shows a simplified model of a balanced transverse comb electrostatic actuator. The proof mass is grounded and the fixed electrodes are biased at V_{tune}. This actuator configuration implements a voltage tunable spring in the transverse direction with stiffness [1]

$$k_e = -\frac{C_{tune}}{x_g^2} V_{tune}^2 \tag{3.7}$$

where x_g and C_{tune} are respectively the gap and net capacitance between the proof mass and the fixed electrodes in the transverse direction when the proof mass is undeflected. The voltage tunable spring combines with other springs suspending the sense axis to yield the net stiffness

$$\begin{aligned} k_s &= k_m + k_e \\ &= k_m - \frac{C_{tune}}{x_g^2} V_{tune}^2 \end{aligned} \tag{3.8}$$

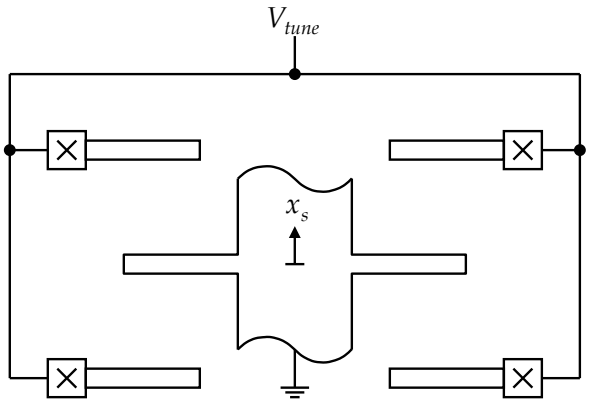

Figure 3.6. Voltage tunable spring implemented by a balanced transverse comb electrostatic actuator.

where k_m is the combined stiffness of the other springs consisting mainly of flextures and parasitic springs from *electrostatic* force feedback and quadrature nulling. Since the tunable spring only softens k_s, it is important to design the flextures to be stiffer than the optimal stiffness by sufficient margin to accommodate force feedback and quadrature nulling induced spring softening in addition to process and ambient variations.

The position sense electrodes are normally realized by transverse combs and thus can double as tuning combs, eliminating the need for a set of electrodes dedicated to stiffness tuning only. Time multiplexing position sensing and stiffness tuning at a sufficiently high rate is one way to share the electrodes. In this case, the effective electrostatic stiffness is scaled by the duty factor of the stiffness tuning phase. From the point of view of minimizing power dissipation, however, a dedicated set of tuning combs is preferable to avoid the typically substantial power penalty associated with charging and discharging the sense capacitors at a high rate.

3.3 Closing the Tuning Loop

The frequency mismatch estimator and voltage tunable spring comprise the necessary elements to implement automatic resonance frequency tuning. The only remaining element is a controller to close the tuning loop. The controller should drive the frequency mismatch estimate to zero and remain stable at all operating points.

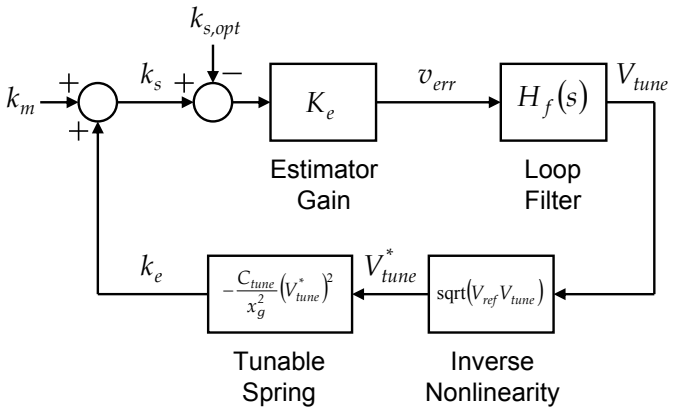

Figure 3.7. Tuning loop with nonlinearity compensation.

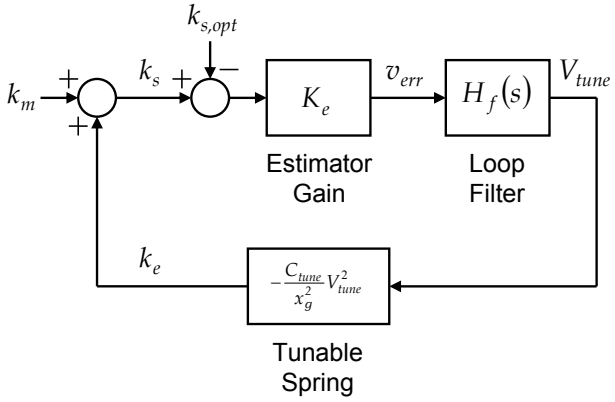

Figure 3.8. Tuning loop without nonlinearity compensation.

The square dependence of the tunable stiffness on voltage results in signal dependent loop gain and must be taken into account in the controller design. Figure 3.7 shows one way to implement the tuning loop. The loop includes an explicit square-root function to counter the square dependence of stiffness on voltage. The open-loop transfer function of the resulting linearized loop is

$$G_{tune} = K_e V_{ref} \frac{C_{tune}}{x_g^2} H_f(s). \tag{3.9}$$

A loop filter with infinite DC gain drives the mismatch to zero.

To simplify system implementation, the square-root may be omitted as shown in Figure 3.8 with the penalty that the loop will exhibit a non-linear settling behavior. The uncompensated square nonlinearity in the loop results in the small-signal open-

loop transfer function

$$G_{tune} = 2\,K_e\,V_{tune}\frac{C_{tune}}{x_g^2}H_f(s) \tag{3.10}$$

which depends on the bias point V_{tune}.

A fundamental property of the proposed estimator is that the mismatch information is modulated onto carriers at $\omega_d \pm \omega_{cal}$. If the mismatch is not constant but time varying, then the modulated signals occupy a non-zero bandwidth. Full recovery of the modulated information is possible provided that their spectral components do not alias. Figure 3.9 illustrates the various possible cases. A unity gain or gain crossover frequency of much less than ω_{cal} allows the loop filter, which can be a simple integrator, enough margin to provide adequate anti-aliasing filtering at ω_{cal} to prevent aliasing and ensure proper loop operation. A higher-order loop filter could provide better attenuation, but the consequent increased phase lag would limit the potential tracking bandwidth improvement. A tracking bandwidth of about 25Hz or settling time constant of about 6ms is possible for $\omega_{cal} = 2\pi \times 250\text{Hz}$.

3.4 Practical Considerations

This section discusses issues regarding practical signal synthesis, demodulation, and filtering, and the effects of finite force feedback open-loop gain and potential interference from large inertial forces.

3.4.1 Practical Signal Synthesis, Demodulation, and Filtering

As shown in Figure 3.10, an offset before the loop filter is indistinguishable from the actual error signal and is consequently a source of systematic frequency offset. Digital implementation of calibration signal synthesis, demodulation, and loop filtering in the experimental prototype avoids the substantial offsets that are possible in analog implementations.

Even with digital implementation, generating a calibration signal with the precise

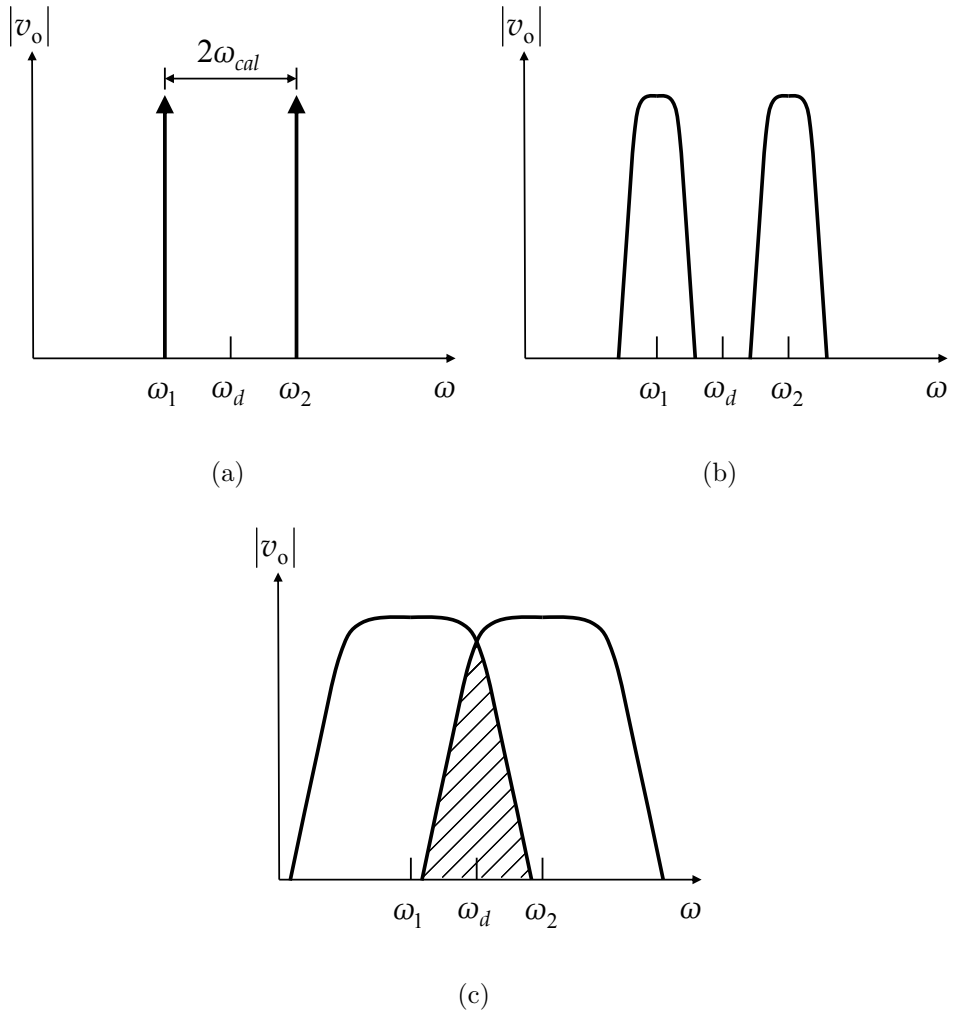

Figure 3.9. Possible spectra of pilot tones modulated by frequency mismatch. (a) Static mismatch is fully recoverable. (b) Dynamic mismatch with variation bandwidth less than ω_{cal} is fully recoverable. (c) Dynamic mismatch with variation bandwidth greater than ω_{cal} resulting in overlapping spectral components is not fully recoverable.

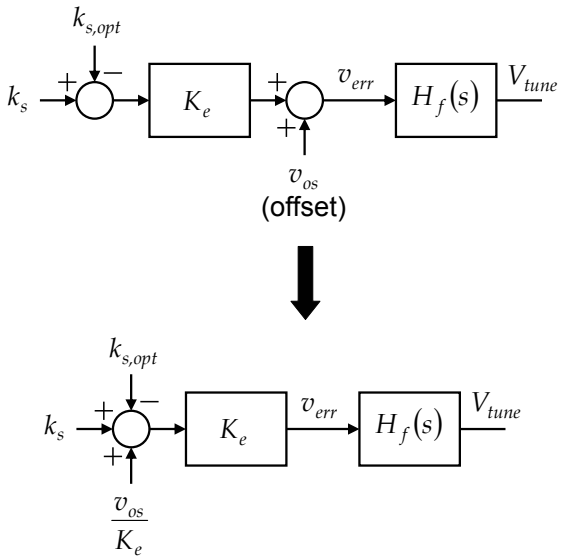

Figure 3.10. Problem of calibration signal, demodulator, and loop filter offset. The lumped offset before the loop filter appears as an equivalent stiffness offset.

amplitude ratio given by (3.6) is inconvenient. Using tones with equal amplitudes is far more convenient and allows the calibration signal to be used directly for demodulation, leading to simpler system implementation as shown in Figure 3.11. With $v_1 = v_2$ and the tone frequencies defined previously, (3.5) becomes

$$v_{err} \propto k_s - m_s\left(\omega_d^2 + \omega_{cal}^2\right) \approx k_s - m_s\omega_d^2\left(1 + \underbrace{\frac{1}{2}\frac{\omega_{cal}^2}{\omega_d^2}}_{\text{offset}}\right)^2 \tag{3.11}$$

where the approximation assumes that $\omega_{cal} \ll \omega_d$ and we have omitted the gain factor for simplicity. Basically, using equal amplitudes introduces a frequency offset that forces the sense resonance frequency to be slightly higher than the drive frequency. Fortunately, the error is negligible relative to signal bandwidth if the tones are located just outside the desired signal band as the following example illustrates. A bandwidth of 50Hz is typical in consumer and automotive applications. Choosing $\omega_{cal} = 2\pi \times$ 250Hz places the pilot tones well outside the desired signal band and, with a drive frequency of 15kHz, results in an offset of 0.013% or 2Hz.

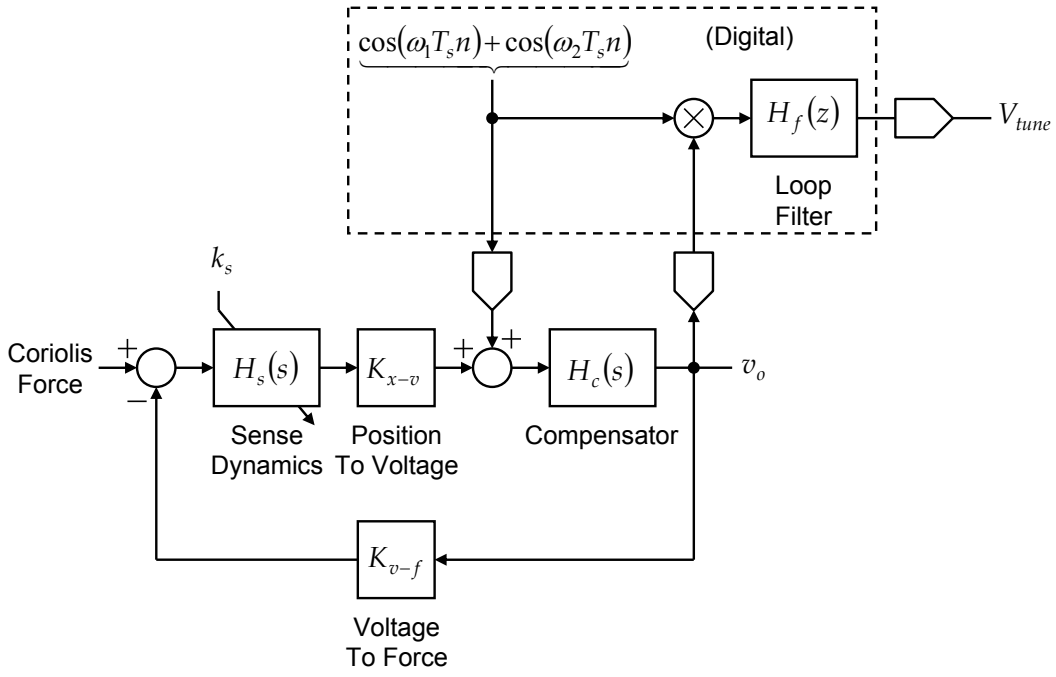

Figure 3.11. Practical estimator with digitally synthesized equal amplitude tones and digitally implemented demodulator and loop filter.

3.4.2 Finite Force Feedback Open-Loop Gain

Since an arbitrarily high open-loop gain is difficult to attain in practice, it is useful to quantify the impact of finite open-loop gain on estimator performance. With finite open-loop gain, the transfer function from the calibration input to the output becomes

$$G_{cal}(s) = \left(1 - \frac{1}{1+T(s)}\right) \frac{1}{K_{v-f}\, K_{x-v}\, H_s(s)} \tag{3.12}$$

where $T(s) = K_{v-f}\, K_{x-v}\, H_s(s) H_c(s)$ is the open loop transfer function, and the in-phase output components become

$$v_{o1,\mathrm{I}} = \left(1 - \frac{\Re\{1+T(j\omega_1)\}}{|1+T(j\omega_1)|^2}\right) \frac{v_1}{K_{v-f}\, K_{x-v}} \left(k_s - m_s\omega_1^2\right) \tag{3.13}$$

and

$$v_{o2,\mathrm{I}} = \left(1 - \frac{\Re\{1+T(j\omega_2)\}}{|1+T(j\omega_2)|^2}\right) \frac{v_2}{K_{v-f}\, K_{x-v}} \left(k_s - m_s\omega_2^2\right). \tag{3.14}$$

The imaginary part of $T(j\omega)$ causes a small portion of the damping term to appear in the in-phase output components. We have neglected this effect for brevity since mode-matching implies a high-Q resonance which, in turn, implies negligible damping.

It is evident from the above equations that finite open-loop gain introduces errors in the tone amplitudes. Only a negligible estimator gain error arises if the amplitude errors in $v_{o1,\mathrm{I}}$ and $v_{o2,\mathrm{I}}$ match, otherwise a frequency offset also arises. Assuming a minimum open-loop gain of T_{min}, the worst case mismatch occurs when $T(j\omega_1) = T_{min}$ and $T(j\omega_2) = -T_{min}$ or vice versa. In this case, the error signal is

$$v_{err} \propto k_s - m_s\left(\omega_d^2 + \frac{2}{T_{min}}\omega_d\omega_{cal}\right) \approx k_s - m_s\omega_d^2\left(1 + \underbrace{\frac{1}{T_{min}}\frac{\omega_{cal}}{\omega_d}}_{\text{offset}}\right)^2. \tag{3.15}$$

Fortunately, the offset is negligible for any reasonable open-loop gain. Continuing with the previous example where $\omega_{cal} = 2\pi \times 250\text{Hz}$, a minimum open-loop gain of 40dB results in a worst case offset of 0.017% or 2.5Hz.

3.4.3 Interference from Large Inertial Forces

Since there is no filter to limit the bandwidth of Coriolis and other inertial forces that appear on the sense axis, spectral components of those forces around $\omega_d \pm \omega_{cal}$ can interfere with the pilot tones and produce signal dependent frequency offset. The use of a tuning fork structure largely rejects the linear acceleration component leaving the Coriolis acceleration component. In the following analysis, we quantify the worst case error that the Coriolis acceleration component can contribute.

The Coriolis acceleration can be expressed as

$$a_c = 2\,\Omega\,\dot{x}_d + \dot{\Omega}\,x_d. \tag{3.16}$$

The $\dot{\Omega}\,x_d$ term captures an often neglected higher order effect that is important in the following analysis. The worst case interference occurs when the angular rate is sinusoidally varying at ω_{cal} in which case the angular rate can be expressed as

$$\Omega = \Omega_0\,\cos(\omega_{cal}t + \phi_\Omega). \tag{3.17}$$

where Ω_0 is the amplitude and ϕ_Ω is the phase which can assume any value. If the drive axis oscillates according to $x_d = x_{d0}\,\cos(\omega_d t)$, then the Coriolis acceleration

resulting from the angular rate is

$$a_c = -\underbrace{2\,\Omega_0\,\omega_d\,x_{d0}\cos(\omega_{cal}t+\phi_\Omega)\sin(\omega_d t)}_{2\,\Omega\,\dot{x}_d} - \underbrace{\Omega_0\,\omega_{cal}\,x_{d0}\sin(\omega_{cal}t+\phi_\Omega)\cos(\omega_d t)}_{\dot{\Omega}\,x_d}. \tag{3.18}$$

The acceleration appears at the output of the force feedback loop scaled by m_s/K_{v-f} (see Figure 3.2). The $2\,\Omega\,\dot{x}_d$ term dominates by far since it is multiplied by ω_d while the $\dot{\Omega}\,x_d$ term is multiplied by the much smaller ω_{cal}. It is therefore important to generate the calibration and demodulation signals by using a sinusoid at ω_{cal} to modulate the amplitude of a carrier that is *in phase* with the drive displacement (and thus *in quadrature* with the drive velocity) to enable the rejection of the dominant $2\,\Omega\,\dot{x}_d$ term. After demodulation, the $\dot{\Omega}\,x_d$ term remains and the error signal becomes

$$v_{err} = K_e\left(k_s - m_s\omega_d^2\right) - \underbrace{\frac{m_s}{K_{v-f}}\Omega_0\,\omega_{cal}\,x_{d0}}_{\text{worst case}}. \tag{3.19}$$

The consequent offset error is minimized by maximizing the estimator gain K_e which requires the use of large amplitude pilot tones. The amplitudes can not be arbitrarily large, however, since the resulting output signals must live within the force feedback loop's limited output range. As we have already seen in Figure 3.4, the output amplitudes of the tones vary substantially with frequency mismatch. Since the amplitudes at worst case frequency mismatch can be substantially higher than with perfect matching, the amplitudes should be small enough to avoid overloading the output during startup when the system has the worst case frequency mismatch. As frequency matching improves, the amplitudes, and consequently the estimator gain, may be increased to minimize the impact of Coriolis interference. It is important to reciprocally lower some other gain factor while increasing estimator gain to maintain an optimal tracking bandwidth. If the pilot tones are maximized, then for full-scale Coriolis acceleration sinusoidally varying at the worst frequency and with the worst phase, the resulting fractional matching error is on the order of $\omega_{cal}^2/\omega_d^2$, which is similar to the magnitude of the other errors.

3.5 Summary

This chapter introduces a technique for detecting and tuning out the mismatch between the drive and sense resonance frequencies of a force balanced gyroscope. The technique estimates the frequency mismatch by injecting out-of-band pilot tones into an appropriate point in the force feedback. Electrostatic spring softening using a balanced transverse comb electrostatic actuator enables the fine tuning of the sense resonance. A loop filter with infinite DC gain drives the mismatch to zero. Digital synthesis of the calibration signal and implementation of the demodulator and loop filter prevents the presence of a large systematic frequency offset. Yet to be presented is the design of the force feedback loop, the crucial element upon which the proposed mode-matching technique depends. The next chapter begins consideration of the design of the force feedback loop with particular focus on the position sense front-end.

Chapter 4

Position Sensing

As discussed in Chapter 2, the position sense front-end sets the electronic noise floor and dominates the power dissipation of the readout interface, and as further discussed, mode-matching is the most effective way to improve the power efficiency of the overall readout interface. Another yet to be explored, but potentially rewarding way is to directly improve the power efficiency of the dominant power dissipator, the position sense front-end. Since feedback in general relaxes certain accuracy requirements of the blocks in the forward path, force feedback presents a special opportunity to trade the well defined and highly linear gain of state-of-the-art front-ends for much lower noise given the same bias current. This chapter focuses on the subject of directly improving the power efficiency of the front-end.

4.1 Force Feedback Loop Stability Consideration

As argued in a previous chapter, force feedback enables effective exploitation of the sense resonance. Unfortunately, with feedback comes the problem of possible closed-loop instability. Previous work has shown that stability at atmospheric pressure is no guarantee of stability in vacuum [10, 11]. The problem is caused by the so far neglected but usually present higher-order resonance modes of the mechanical structure arising from resonances of the suspension or electrostatic drive and sense comb fingers for

example. While normally over-damped at atmospheric pressure, these modes are highly under-damped in vacuum where they destabilize loops employing traditional lead compensation [12].

The force feedback loop is said to employ collocated control if position sensing and force feedback share the same set of electrodes. Conversely, it is said to employ non-collocated control if they each use dedicated electrodes. In the latter case, the dynamics between the position sensing and force feedback electrostatic comb fingers introduce additional unwelcome phase lag into the response of the mechanical structure [13]. Figure 4.1 illustrates the frequency responses that are possible under both configurations with a higher-order resonance at 100kHz. The *flipping* of the ordering of the resonance and anti-resonance, possible only in the case of non-collocated control, results in the phase lag approaching 360° near the second resonance peak. Collocated control is preferable since it guarantees the presence of a phase restoring anti-resonance between any pair of successive resonances. The anti-resonance prevents the phase lag from exceeding 180° near resonance peaks and thereby facilitates force feedback loop compensation.

While frequency-multiplexing position sensing and force feedback onto the same set of electrodes realizes collocated control [8], the inherently continuous-time technique requires the use of proportional feedback which complicates the task of mode-matching as will be explained in the next chapter. Bang-bang feedback avoids the complication but is only possible if time-multiplexing is used. The discontinuous-time operation inherent in time-multiplexing implies the use of a sampling front-end.

4.2 Sampling and Noise Folding

Figure 4.2 shows the traditional front-end used to convert an imbalance between the sense capacitors to voltage [14]. Based on charge integration, the front-end uses a wideband capacitive feedback amplifier to provide a highly accurate gain that is insensitive to ambient variations. During the position sensing phase of the time-multiplexing operation, a voltage pulse is applied on the proof mass node. The resulting transfer of charge from the sense capacitors to the integration capacitors

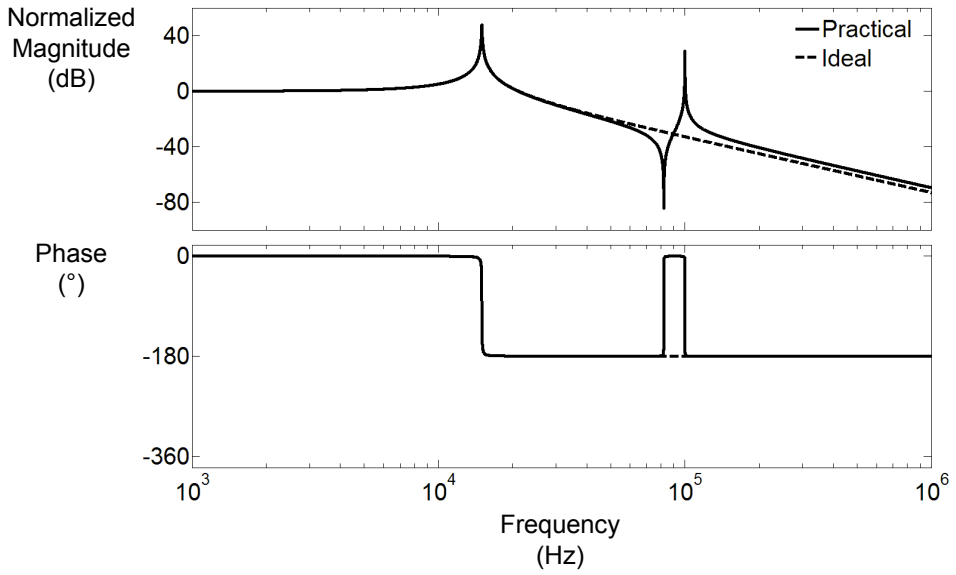

(a)

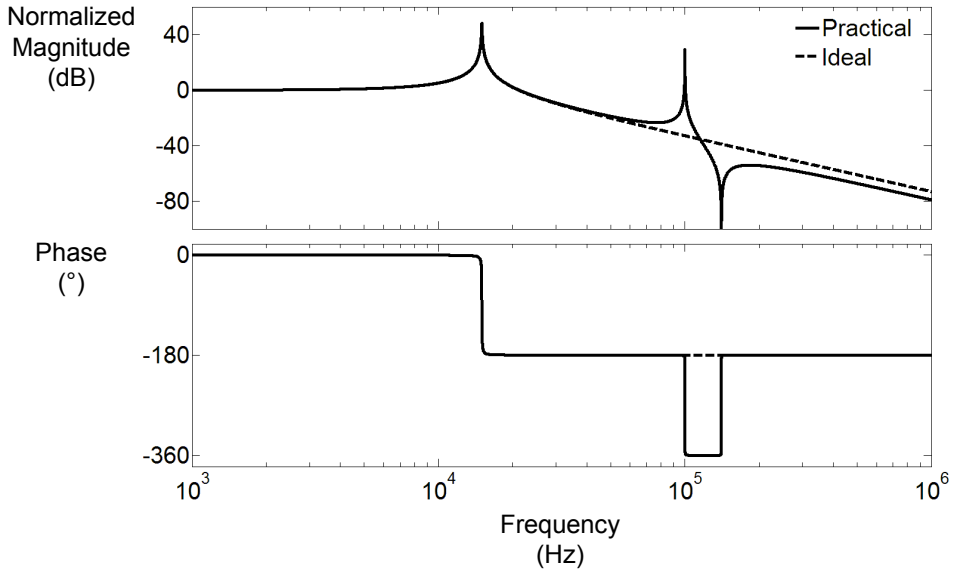

(b)

Figure 4.1. Typical sensor frequency response under (a) collocated control and (b) non-collocated control. The dashed lines indicate the ideal second-order response.

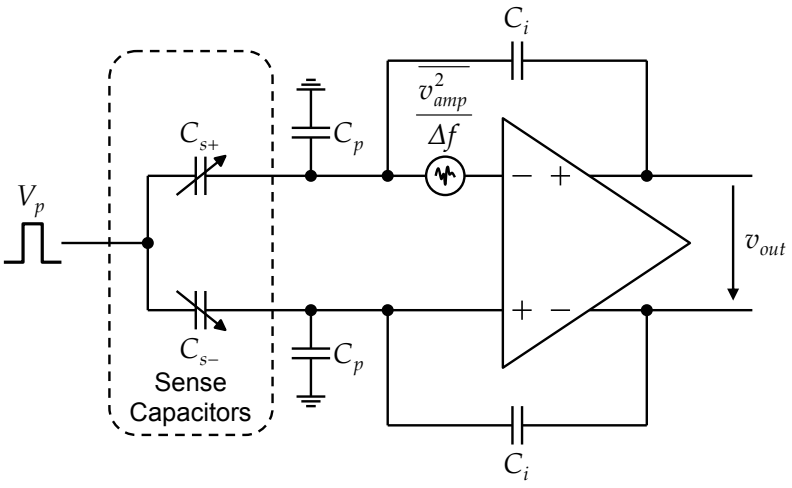

Figure 4.2. Differential charge integrator front-end.

(C_i) gives rise to a differential output signal whose magnitude is proportional to the imbalance between the sense capacitors. The wide bandwidth, typically several times the Nyquist rate, is imperative for the complete transfer of charge. The output of the amplifier must be sampled and held to ensure its availability for further processing during subsequent phases when the sense capacitors are scheduled for operations other than position sensing. Since sampling a continuous-time signal causes the spectral components at multiples of the Nyquist frequency to *fold* down into the baseband, the wide bandwidth of the amplifier leads to substantial folding of the input referred thermal noise of the amplifier and consequent degradation of SNR offset only by increased bias currents [15]. Figure 4.3 illustrates this problem.

On a broader perspective, the often expressed perception that noise folding is absent in systems employing continuous-time front-ends is valid only if high-order anti-aliasing filtering precedes the signal sampling performed in systems producing digital output. With a high-order anti-aliasing filter, however, the continuous-time design loses its power advantage. Noise folding is therefore a problem general to interfaces generating digital (sampled) output and is not peculiar to the architecture proposed in this work.

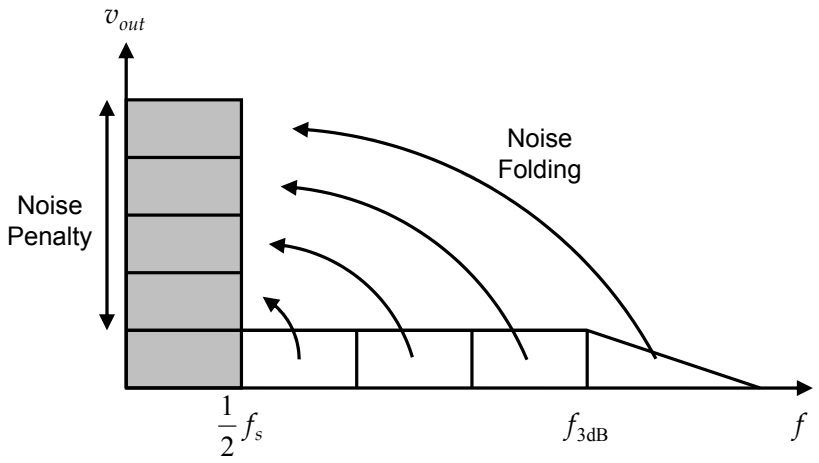

Figure 4.3. Amplifier noise folding.

4.3 Boxcar Sampling

The proposed front-end uses boxcar sampling to minimize amplifier noise folding. Figure 4.4 illustrates the operating principle. The sampler, shown as single-ended for simplicity, produces each sample by integrating the input signal over a fixed time window. The subsequent stage (not shown) uses only the value of the output at the end of the integration phase, then the output is reset in preparation for the next integration phase. The output voltage at the end of the integration phase is

$$v_{out}(nT_s) = \frac{1}{C_L}\int_{nT_s-T_{int}}^{nT_s} G_m v_{in}(t)dt \tag{4.1}$$

where C_L is the load capacitance and T_{int} is the duration of the integration phase. The windowed integration is equivalent to filtering using a boxcar filter with the transfer function

$$H_{box}(s) = \frac{1-e^{-sT_{int}}}{s}\frac{G_m}{C_L}. \tag{4.2}$$

Figure 4.5 compares the frequency response of the boxcar filter and that of a charge integrator with a time constant that is a tenth of the settling time. We set the settling time equal to T_{int} for a fair comparison. The early roll-off and periodic nulls of the sinc response of the boxcar filter provide superior anti-aliasing filtering. The input referred noise of the amplifier, represented by the white noise generator with spectral density $\overline{v_{amp}^2}/\Delta f$, appears at the output filtered by $H_{box}(s)$. The variance of the

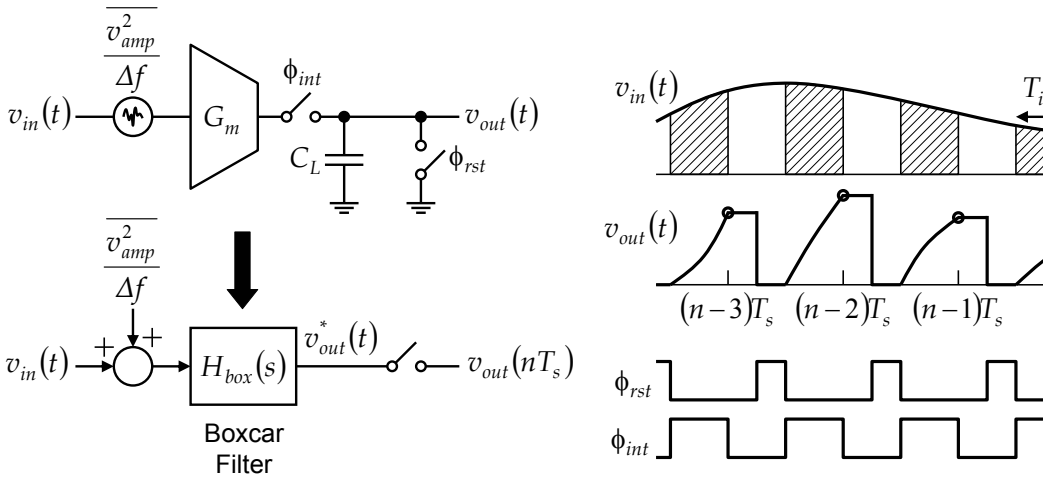

Figure 4.4. Operating principle of boxcar sampler. The output is obtained by integrating the segments of the input over the hashed lines.

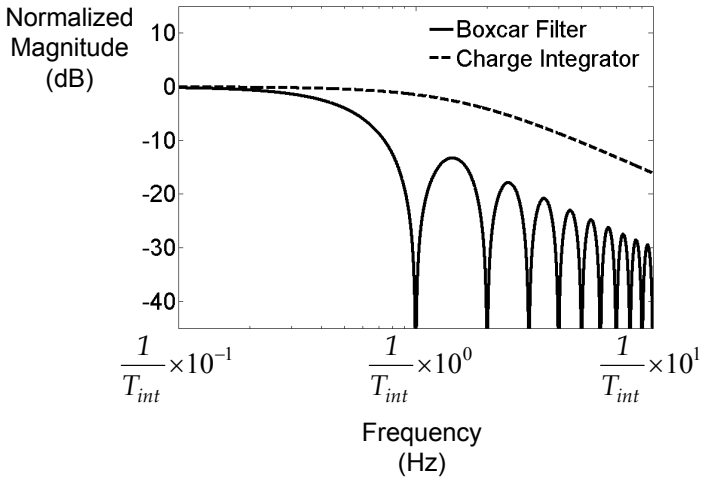

Figure 4.5. Normalized frequency responses of a boxcar filter and a charge integrator from the noise input to the output. The integration phase duration of T_{int} results in a boxcar filter noise bandwidth of $0.5/T_{int}$ (Hz). The charge integrator is assumed to have a first order settling time constant of $0.1 \times T_{int}$ resulting in a noise bandwidth of $2.5/T_{int}$ (Hz) which is five times larger than that of the boxcar filter.

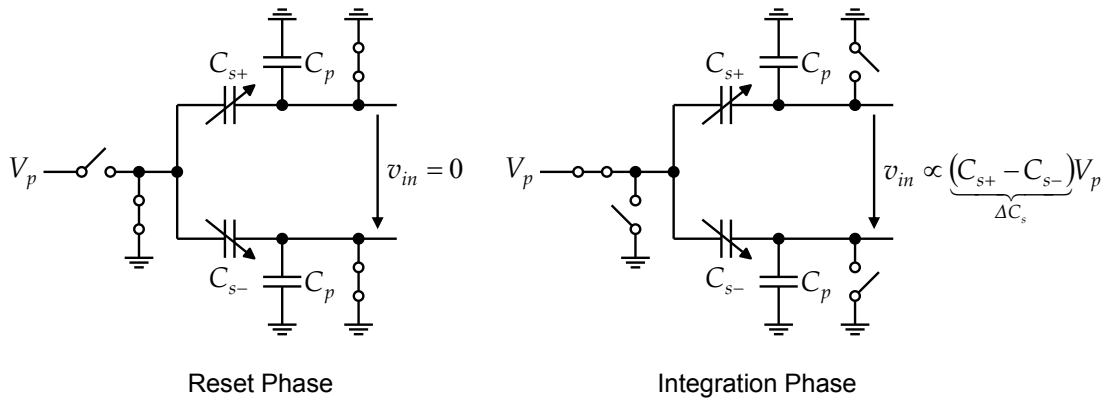

Figure 4.6. Gm-C integrator input voltage generation.

resulting output noise is

$$\begin{aligned} \overline{v_n^2} &= \int_0^\infty H_{box}(j2\pi f) H_{box}^*(j2\pi f) \frac{\overline{v_{amp}^2}}{\Delta f} df \\ &= \frac{1}{2} \frac{\overline{v_{amp}^2}}{\Delta f} \frac{G_m^2 T_{int}}{C_L^2} \end{aligned} \tag{4.3}$$

where we have used the fact that $\int_0^\infty \mathrm{sinc}^2(f) df = \frac{\pi}{2}$. The wiring resistance of the sense element also contributes thermal noise that is often non-negligible. This noise also appears at the output filtered by $H_{box}(s)$. We have neglected the kT/C noise that appears on the load capacitor after the reset switch is opened since that switch is included in this discussion only for clarity and is absent from the experimental prototype.

Figure 4.6 shows how to generate the input voltage of the Gm-C integrator. Variable capacitors C_{s+} and C_{s-} represent the displacement sensitive sense capacitors. They have a nominal value of C_{s0} when the proof mass is in the balanced position. The other capacitors represent the parasitic capacitances of the sense element and transconductance amplifier. During the reset phase, the proof mass and the sense nodes of the sense element are grounded. At the beginning of the integration phase, the sense nodes are released, and the proof mass node is switched to V_p, causing the voltages on the now floating sense nodes to shift. If there is an imbalance between C_{s+} and C_{s-}, then a voltage proportional to the imbalance appears across

the sense nodes with the value

$$\begin{aligned} v_{in} &= (V_p - V_{cm}) \frac{\Delta C_s}{C_{s0} + C_p} \\ &= \left(1 - \underbrace{\frac{C_{s0}}{C_{s0} + C_p}}_{\text{gain error}} \right) \frac{\Delta C_s}{C_{s0} + C_p} V_p \end{aligned} \tag{4.4}$$

where $\Delta C_s = C_{s+} - C_{s-}$. The shift in the common mode voltage of the sense nodes reduces the effective voltage across the sense capacitors, causing a gain error that can be minimized using common-mode feedback (CMFB). In our implementation, we forgo CMFB to avoid the additional power dissipation and loading of the sense nodes by the CMFB circuit since in the experimental prototype, the parasitic capacitance dominates over the sense capacitance, resulting in only a modest common-mode shift.

The voltage given by (4.4) is subsequently boxcar sampled. Since the imbalance between C_{s+} and C_{s-} is essentially static within the relatively short integration interval, the time integration performed by the boxcar sampler reduces to multiplication by the integration time, and thus

$$\begin{aligned} v_{out} &= \frac{G_m T_{int}}{C_L} v_i \\ &= \frac{G_m T_{int}}{C_L} \left(1 - \frac{C_{s0}}{C_{s0} + C_p} \right) \frac{\Delta C_s}{C_{s0} + C_p} V_p. \end{aligned} \tag{4.5}$$

Comparing the SNR of the boxcar sampler and switch-capacitor charge integrator for the same bias current helps quantify the relative merits of the two techniques. In the charge integrator (see Figure 4.2), the input referred noise of the amplifier appears at the output with variance [14]

$$\overline{v_{n,sc}^2} = \frac{1}{4} \frac{\overline{v_{amp}^2}}{\Delta f} \left(\frac{C_{s0} + C_i + C_p}{C_i} \right)^2 \frac{1}{\tau_{amp}}. \tag{4.6}$$

where C_i and τ_{amp} are respectively the integration capacitance and settling time constant of the amplifier, and an imbalance in the sense capacitors results in the output voltage

$$v_{out,sc} = \left(1 - \frac{C_{s0}}{C_{s0} + C_i + C_p} \right) \frac{\Delta C_s}{C_i} V_p. \tag{4.7}$$

The ratio of the SNR of the two techniques is

$$\begin{aligned}
\frac{\mathrm{SNR_{box}}}{\mathrm{SNR_{sc}}} &= \frac{\left(\frac{v_{out}^2}{\overline{v_n^2}}\right)_{box}}{\left(\frac{v_{out}^2}{\overline{v_n^2}}\right)_{sc}} \\
&= \frac{1}{2}\frac{T_{int}}{\tau_{amp}}\frac{1}{(1-F)^2\left(1+\frac{C_{s0}}{C_p}F\right)^2} \\
&\approx \underbrace{\frac{1}{(1-F)^2}}_{\substack{\text{feedback}\\ \text{penalty}}}\underbrace{\frac{n_\tau}{2}}_{\substack{\text{settling}\\ \text{penalty}}}
\end{aligned} \tag{4.8}$$

where $F = C_i/\left(C_{s0}+C_i+C_p\right)$ and $n_\tau = T_{int}/\tau_{amp}$ are respectively the feedback factor and number of settling time constants of the switch-capacitor amplifier. The approximation is valid for the case where the parasitic capacitance dominates. The first factor captures the noise penalty resulting from using feedback in the SC solution. The second term accounts for the high amplifier bandwidth needed for settling. For typical implementations, the boxcar sampler achieves about an order magnitude better SNR than a typically designed switch-capacitor charge integrator.

In the preceding discussion, we neglected the kT/C noise that is stored on the sense nodes upon the release of those nodes. For the SNR advantage derived above to be true, the front-end must be able to cope with this kT/C noise and the $1/f$ noise of the transconductance amplifier implementing the Gm-C integrator.

4.4 Removing Switch kT/C Noise and Amplifier $1/f$ Noise

The sense nodes are connected to feedback voltages during the force feedback phase to realize the previously described collocated control, and thus must be reset to ground (or another voltage within the input common-mode range of the transconductance amplifier) in preparation for the integration phase. Those reset switches are therefore unavoidable. Fortunately, the error from the consequent kT/C noise can be removed by the same technique used to address $1/f$ noise since the error stays frozen in time once the switches are opened.

Correlated double sampling (CDS) is a technique used to remove or attenuate the effects of time-correlated noise in sampling front-ends [16, 17, 18]. It operates by subtracting a sample of the input containing only noise from a temporally close sample containing both signal and noise. The subtraction substantially removes the slowly varying noise. Figure 4.7 shows how we extend CDS to the boxcar sampling front-end. CDS operation starts with a reset phase, followed by an error integration phase of duration T_{int}, then an error and signal integration phase of duration T_{int} in which the proof mass node is switched to V_p. The sense nodes are released to float during both integration phases. To realize the subtraction, the output current of the transconductance amplifier is integrated with negative polarity during the error integration phase, and positive polarity during the error and signal integration phase. Output current inversion is realized by cross connecting the output nodes of the transconductance amplifier to the load capacitors.

Figure 4.8 shows a system representation of the CDS operation. The error during the error integration phase is delayed by T_{int} and subtracted from the error and signal during the error and signal integration phase. As before, the signal is filtered by only $H_{box}(s)$, but the kT/C noise is entirely removed since the error is the same in both integration phases; the $1/f$ noise is additionally filtered by $1-e^{-sT_{int}}$, a differentiator whose magnitude response is $2\sin(\pi f T_{int})$. Suppose $T_{int} = 1\mu$s, then at the drive frequency of 15kHz, the differentiator provides about 20dB of $1/f$ noise rejection.

Similar to traditional CDS implementations, noise rejection is achieved at the cost of doubling the thermal component of the output noise since the thermal noise of the amplifier and wiring resistance of the sense element are sampled twice.

4.5 Other Practical Considerations

The lack of electronic feedback leaves the proposed front-end potentially more susceptible to the adverse effects of imperfections such as integration time jitter and drift, transconductance variation, and nonlinear device characteristics. This section evaluates, within the context of force feedback, the effects of such imperfections on the performance of the front-end.

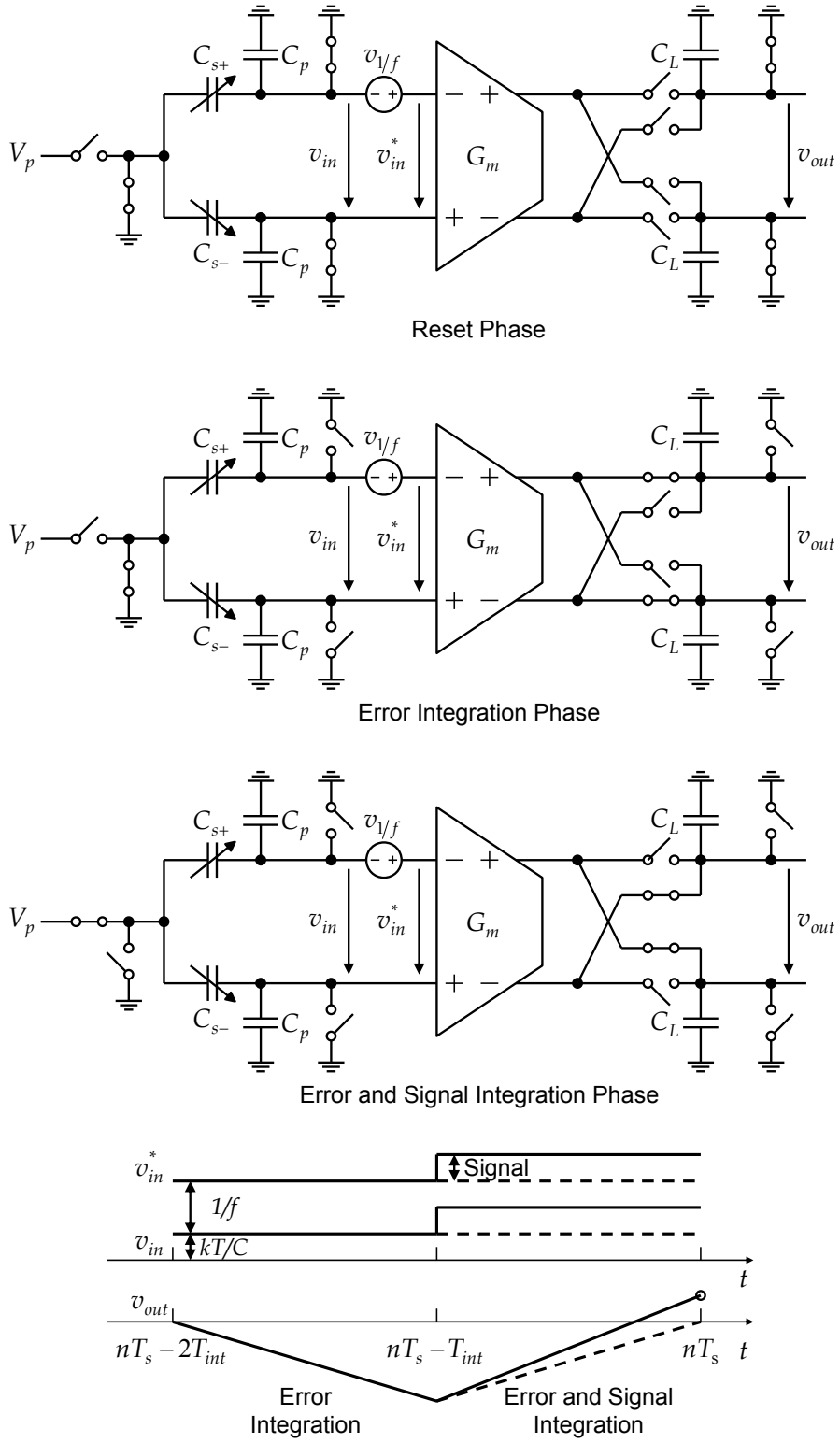

Figure 4.7. Correlated double sampling operation of boxcar sampler.

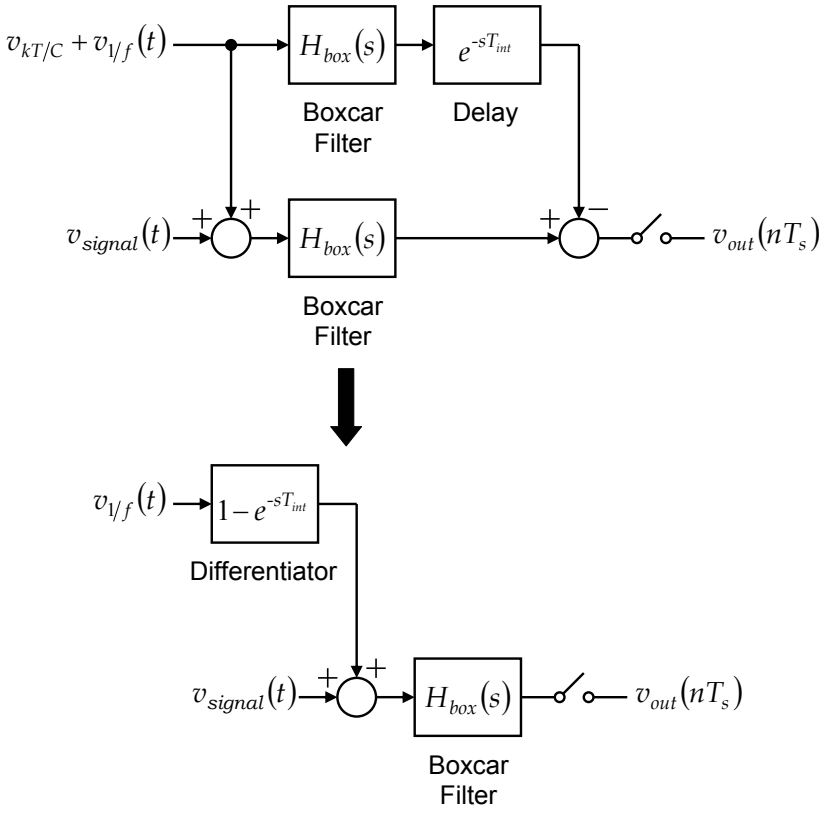

Figure 4.8. System representation of correlated double sampling operation of boxcar sampler. The kT/C noise is entirely removed, and the $1/f$ noise is additionally filtered by a differentiator.

Suppose the integration time is nominally T_{int} with a small variation ΔT_{int}, then

$$v_{out} = \frac{G_m T_{int}}{C_L} v_{in} \left(1 + \underbrace{\frac{\Delta T_{int}}{T_{int}}}_{\text{error}} \right). \tag{4.9}$$

Similar to how force feedback rejects the error due to the sense mode quality factor drift, force feedback rejects the error resulting from the slow drift of the integration time. Of concern is the random jitter, which mixes with v_{in} to produce a random error. To avoid degrading the intrinsic noise floor of the amplifier, the variance of the error should be well below the RMS noise of the amplifier or

$$\overline{v_{in}^2} \overline{\left(\frac{\Delta T_{int}}{T_{int}} \right)^2} \ll \frac{\overline{v_{amp}^2}}{\Delta f} \frac{f_s}{2}. \tag{4.10}$$

where f_s is the system sampling rate. In the experimental prototype, $\overline{v_{amp}^2}/\Delta f = \left(70\text{nV}/\sqrt{\text{Hz}} \right)^2$ and $f_s = 480\text{kHz}$ resulting in an RMS noise of $48\mu\text{V}$. Thanks to force feedback, the full-scale v_{in} in the experimental prototype is only on the order of 5mV. Assuming an RMS jitter of 100ppm, which is very easy to achieve, the variance of the resulting error is 500nV, two orders of magnitude lower than the intrinsic amplifier noise.

Transconductance variation, due, for example, to bias current noise and drift, also gives rise to dynamic gain variation. The nonlinearity of the differential pair used to realize the transconductance amplifier results in additional signal dependent errors. As in the case of integration time jitter and drift, the very small input signal level keeps the resulting errors well within acceptable limits.

4.6 Summary

The traditional position sense front-end suffers from substantial noise folding resulting in the degradation of SNR offset only by increased bias currents. This chapter proposes boxcar sampling as a way to minimize the noise folding and thereby achieve significantly higher SNR for the same bias current. Force feedback was proposed in Chapter 2 as a means to increase the tolerance for process and ambient variations of the sense element. This chapter extends the idea to the next block in the forward

path, the front-end, to enable an order of magnitude improvement in SNR above and beyond that derived from mode-matching. The next chapter builds upon the discussion begun in this chapter on force feedback loop design.

Chapter 5

Force Feedback

Force feedback is key to effectively exploiting mode-matching and boxcar sampling for several orders-of-magnitude reduction in overall interface power dissipation. In the design of the force feedback loop, care must be taken to avoid design choices that conflict with mode-matching or leave the system susceptible to closed-loop instability. This chapter focuses on the design of the force feedback loop with particular emphasis on minimizing analog complexity and power while addressing the above concerns.

5.1 Mode-Matching Consideration

Figure 5.1 shows how to drive the proof mass and position sense electrodes during the force feedback phase to realize differential actuation. The proof mass is grounded, and the top and bottom electrodes are biased at V_{bias} and driven differential by the feedback voltage v_{fb}. In another approach, the top and bottom electrodes are biased at V_{bias} and $-V_{bias}$ respectively and the proof mass is driven by v_{fb}. Both approaches produce similar results. However, the first approach is preferable since it requires only one bias voltage. In any case, the feedback force applied on the proof mass for

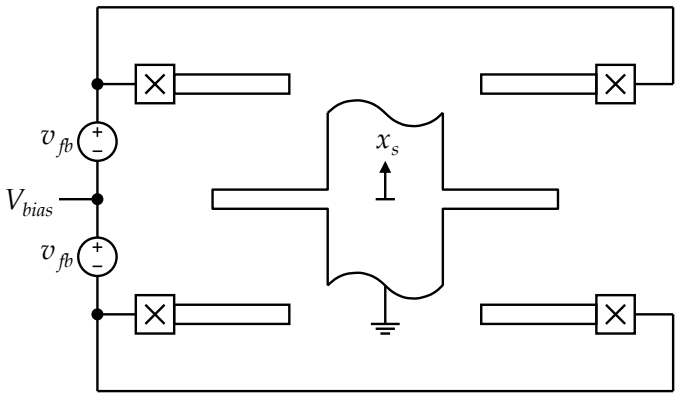

Figure 5.1. Schematic diagram of the sense combs doubling as differential actuator.

displacements that are small relative to the gap is [1]

$$F_{fb} = \underbrace{2\frac{C_{s0}}{x_g}V_{bias}}_{K_{v-f}} v_{fb} + \underbrace{2\frac{C_{s0}}{x_g^2}\left(V_{bias}^2 + v_{fb}^2\right)}_{\substack{\text{signal dependent} \\ \text{stiffness}}} x_s \tag{5.1}$$

where x_g is the nominal gap and C_{s0} is the nominal sense capacitance between the proof mass and each pair of connected electrodes. In addition to the desired voltage controlled force with a voltage-to-force gain of K_{v-f}, the transducer produces an unwanted stiffness term that also depends on the feedback voltage. During normal operation, the tuning loop forces the pilot tones used for resonance frequency calibration to have equal amplitudes at the output of the force feedback loop. Neglecting other signals that may be present and assuming that proportional feedback is used, the output signal will be of the form $\cos\left[(\omega_d - \omega_{cal})t\right] - \cos\left[(\omega_d + \omega_{cal})t\right] = 2\sin(\omega_{cal}t)\sin(\omega_d t)$. The feedback voltage is derived from the output and thus can be expressed as $v_{fb} = |v_{fb}|\sin(\omega_{cal}t)\sin(\omega_d t)$. The square of this voltage modulates the signal dependent stiffness term resulting in spectral components at DC in addition to $2\omega_{cal}$, $2\omega_d$, and $2\omega_d \pm 2\omega_{cal}$. While the DC component will be removed by the tuning loop, the AC components, all of which are beyond the tracking bandwidth of the tuning loop, will remain. Additional signals in the output, the Coriolis force for example, exacerbate the problem. Left unaddressed, the parasitic tuning of stiffness by the feedback voltage would result in about 1% dynamic variation of the sense resonance in the experimental prototype.

Bang-bang control, a feedback control strategy in which the feedback voltage is

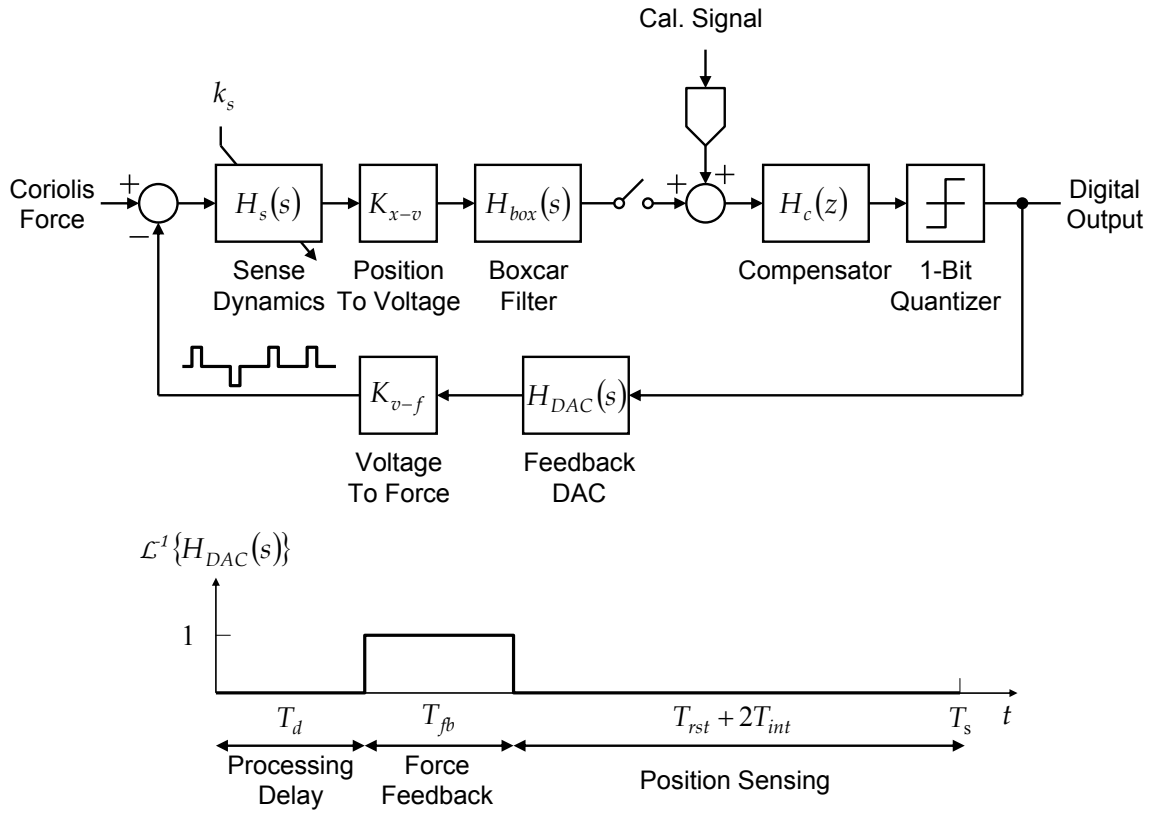

Figure 5.2. Preliminary system architecture. The time $T_{rst} + 2T_{int}$ accounts for the reset, error integration, and error and signal integration phases of position sensing.

restricted to just two levels, say $\pm V_{bias}$, overcomes this problem. With bang-bang control, the feedback voltage toggles between V_{bias} and $-V_{bias}$ in such a way that its time-average approximates the feedback voltage under proportional control. The technique converts the dynamic frequency variation into a static error since, regardless of the spectral content of the feedback voltage, the square is constant, V_{bias}^2. The resulting static error is removed by the tuning loop.

5.2 Preliminary System Architecture and Model for Stability Analysis

Figure 5.2 summarizes the preliminary system architecture. To realize the above mentioned bang-bang control, a single-bit quantizer placed after the compensator

restricts the feedback voltage to just two levels resulting in an architecture akin to a $\Sigma\Delta$ modulator with the noise shaping realized by the sense element complemented by the compensator [19, 14, 20, 21, 22, 23]. The inherent analog-to-digital conversion obviates the need for a dedicated high resolution A/D following the output, and the single-bit output facilitates implementation of the mode-matching algorithm by reducing the demodulator to a simple multiplexer that either keeps or inverts the sign of the demodulation signal. The boxcar filter captures the behavior of the front-end proposed in the previous chapter. The impulse response of the feedback DAC accounts for the time-multiplexing of force feedback onto the position sense electrodes. The delay to the beginning of the pulse accounts for the time it takes the compensator and quantizer to process the position signal and produce the next output. As required by the mode-matching algorithm, a DAC for injecting the calibration signal is included.

A major design goal is ensuring that the system is stable in the sense that the digital output is free of large limit cycles and is a faithful representation of the Coriolis force. The presence of the quantizer results in a complex system behavior that is hard to analyze directly. The describing function model, a widely used approximation in which the nonlinear element is replaced with a signal-dependent gain and an additive noise source [24], captures sufficient detail of the nonlinear behavior under certain conditions to yield valuable insight into the nature of instability in the modulator [25]. Figure 5.3 shows the describing function model for evaluating the robustness of various compensation schemes. To further facilitate the analysis, we have also replaced the electromechanical chain with its impulse invariant discrete-time equivalent [10].

5.3 Accommodating Parasitic Resonances

While the linear model above does not identify sufficient conditions for stability, it has been found via simulation that the lack of phase margin in the model is a sufficient condition for instability. We use this powerful capability in the following analysis to evaluate the robustness of various compensation schemes.

Although practical gyroscopes typically have countless resonance modes across a wide range of frequencies, we consider for simplicity a hypothetical sensor with only

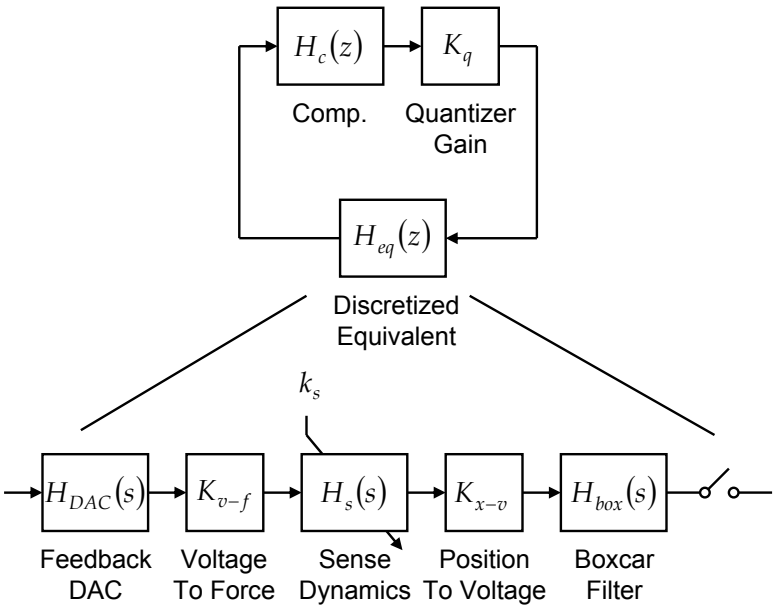

Figure 5.3. Model for evaluating the robustness of various compensation schemes.

one parasitic resonance at 300kHz in addition to a main resonance at 15kHz. Figure 5.4 shows the frequency response of the sensor along with that of the discretized electromechanical chain for a sampling rate of 480kHz. Since collocated control ensures the presence of a phase restoring anti-resonance between successive resonances, the continuous-time phase response does not cross the -180° threshold. However, the parasitic resonance, being in the second Nyquist zone, aliases down with a very large excess phase lag since signals in even Nyquist zones alias with inverted phase. Unfortunately, increasing the sampling rate to bring all resonances below the Nyquist frequency is both impractical and ineffective. It is impractical because the sense and parasitic capacitances and the wiring resistance of real sensors impose time constants that limit the maximum sampling rate. It is ineffective because the processing delay together with other delays in the electromechanical chain introduce additional phase lag that pushes the discretized phase response well below -180° even in the absence of parasitic resonances. The very large excess phase lag in the example is therefore a fairly common occurrence. We now evaluate the abilities of various compensation schemes to accommodate parasitic resonances with such excess phase lag.

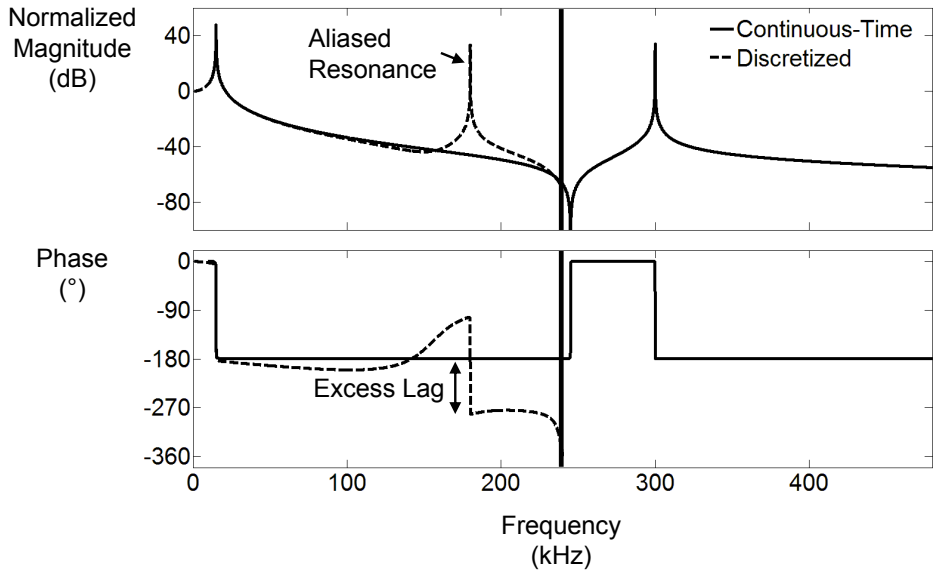

Figure 5.4. Frequency responses of a sensor with a parasitic resonance at 300kHz that aliases down to 180kHz with increased excess phase lag in the discretized frequency response.

5.3.1 Traditional Lead Compensation

Readout interfaces employing $\Sigma\Delta$ force feedback must reject the quantization noise in the desired signal band to a very high degree to satisfy stringent resolution requirements. Because the frequency shaping provided by the sense element alone is always insufficient to reject quantization noise to a level below that set by the position sense front-end [10], the widely used second-order modulator, the architecture in which the sense element is the sole provider of frequency shaping and the compensator only supplies phase lead, always has a degraded SNR. The degradation can be quite substantial, for example 20dB in [23]. It is possible to realize a second-order architecture that avoids the SNR degradation by using multi-bit rather than single-bit quantization. Among the disadvantages of this approach are the difficulty of applying the required multi-bit force-feedback in a way that is compatible with the previously mentioned bang-bang control, the increased complexity of the demodulator used by the mode-matching algorithm, and the increased complexity of the decimator used to process the oversampled multi-bit output. Additional frequency shaping provided by the compensator in the fourth-order modulator reported in [22] eliminates the SNR

degradation with minimal added complexity. We consider only the forth-order architecture since it preserves the SNR improvements with only a very modest increase in the overall system complexity.

The compensator used in the fourth-order architecture is of the form

$$H_c(z) = \underbrace{\frac{z+a}{z}}_{\substack{\text{lead}\\ \text{comp.}}} \underbrace{\frac{z^2+b_1 z+b_2}{z^2+cz+1}}_{\substack{\text{frequency}\\ \text{shaping}}}. \tag{5.2}$$

The pair of imaginary poles controlled by c provides the above mentioned frequency shaping, and the pair of complex zeros controlled by b_1 and b_2 compensates the phase lag of the imaginary poles. The zero at a provides phase lead at high frequencies to compensate the phase lag of the discretized system. The pole at the origin, unavoidable since a physically realizable system cannot have more zeros than poles, unfortunately negates the phase lead provided by the zero, limiting the available phase lead near the Nyquist frequency. Figure 5.5 shows the resulting open-loop frequency response for typical coefficient values. As one might expect, the system is stable without the parasitic resonance. With the parasitic resonance, however, the system possesses three unity gain frequencies the last of which is characterized by a large negative phase margin. Unfortunately, the system cannot be stabilized by simply lowering the overall gain since doing so introduces negative phase margin at a different frequency. Even after lowering the gain to a point where the available in-band loop gain is far too low to be useful, the system remains unstable. Lacking the large phase lead needed to accommodate high-Q parasitic resonances, compensators of this kind are inadequate for practical vacuum packaged gyroscopes.

5.3.2 Positive Feedback Technique

A block whose output is simply the negative of the input is normally thought of as introducing 180° of phase *lag* at all frequencies. Equally valid is thinking of the block as introducing 180° of phase *lead* at all frequencies since $e^{\pm j\pi} = -1$. The 180° of phase lead is free to be exploited provided that the consequent positive feedback is handled with care. To prevent the positive feedback from leading to instability, the open-loop DC gain must be set below unity and a lag compensator must be included

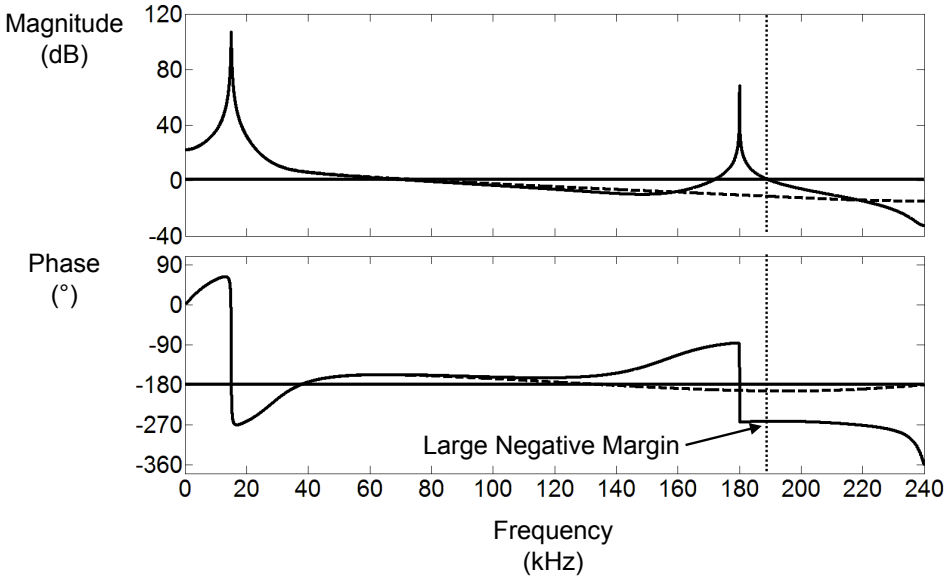

(a)

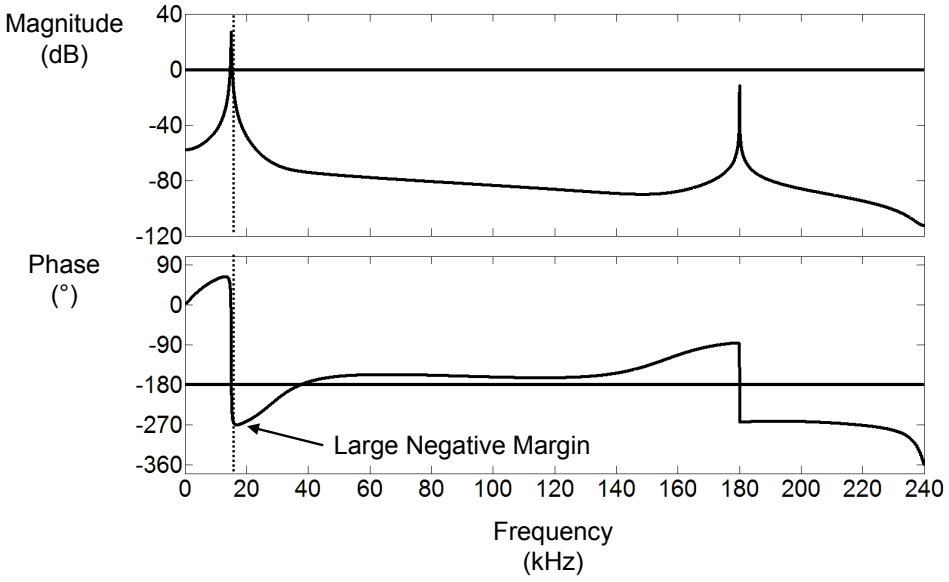

(b)

Figure 5.5. Open-loop frequency response of a forth-order modulator with a parasitic resonance. (a) The system is unstable since there is no phase margin at the third unity gain frequency. (b) Lowering the gain introduces negative phase margin at a different frequency and therefore fails to stabilize the system. The dashed lines indicate the ideal response.

to provide adequate phase margin at the first unity gain frequency. Note that we have expanded the definition of phase margin to mean the minimum margin to $\pm 180°$, not just the traditionally used $-180°$. An open-loop DC gain below unity, effectively resulting in the absence of force feedback at DC, is permissible in this application since the Coriolis force is away from DC. With these adjustments and the inclusion of frequency shaping, the form of the compensator becomes

$$H_c(z) = -\underbrace{\frac{z}{z+a}}_{\substack{\text{lag}\\ \text{comp.}}} \underbrace{\frac{z^2+b_1 z+b_2}{z^2+cz+1}}_{\substack{\text{frequency}\\ \text{shaping}}}. \tag{5.3}$$

The minus sign provides the *automatic* $180°$ of phase lead. The pole at a provides the above mentioned phase margin at the first unity-gain frequency. The zero at the origin is added to cancel the phase lag contributed by the pole at high frequencies since potential parasitic resonances at those frequencies, having substantial phase lag themselves, require no additional lag compensation. In similarity to the previously considered compensator, the pair of complex zeros compensates the phase lag of the pair of imaginary poles included to provide the necessary frequency shaping. Figure 5.6 shows the resulting open-loop frequency response for typical coefficient values. The compensator provides ample phase margins for the parasitic resonance. The margin at low frequencies, though small, is enough for stability. Figure 5.7 shows the root locus of the system. Except for the real pole of the compensator which exits the unit circle for open-loop DC gains greater than unity, all the-closed loop poles stay within the unit circle at all gains. Setting the open-loop DC gain below unity with some safety margin guarantees stability. The guarantee of stability for all open-loop DC gains below unity implies that the modulator will always recover from an overload condition since overload only reduces the open-loop DC gain. With these assurances of stability, parasitic resonances can be safely neglected.

A major drawback of this compensation scheme is that the open-loop gain cannot be increased arbitrarily by including yet additional imaginary pole pairs since the entire phase space from $+180°$ to $-180°$ has already been consumed by the phase lag coming from the imaginary poles of the sensor and the compensator (see Figure 5.6). Since, as discussed in Chapter 3, the accuracy of the mode-matching algorithm depends on the open-loop gain at the pilot tone frequencies, it is important to verify that the open-loop gain resulting from the use of this scheme is sufficient. The

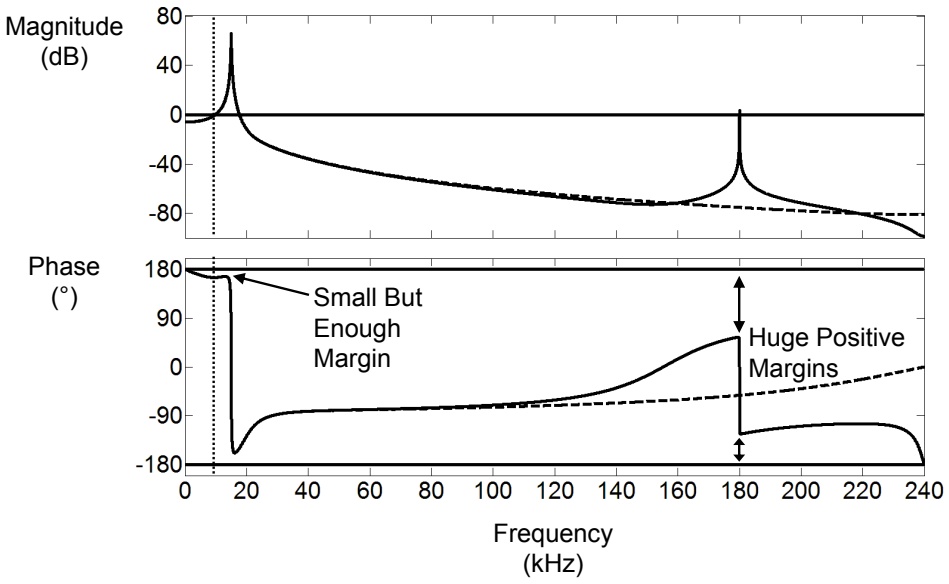

Figure 5.6. Open-loop response of the positive feedback compensated loop.

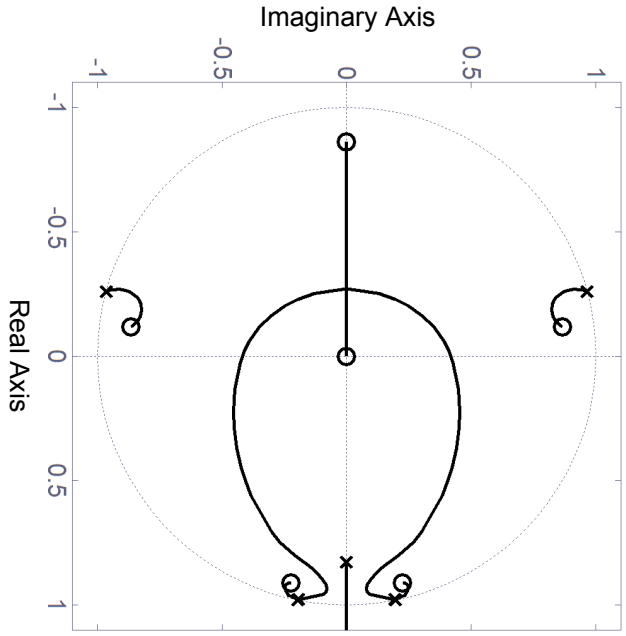

Figure 5.7. Root locus of the positive feedback compensated loop. The high frequency imaginary poles are due to the parasitic resonance. One of the two pairs of low frequency imaginary poles comes from the sensor. The other pair and the real pole come from the compensator.

maximum achievable open-loop gain at a frequency offset Δf from the drive frequency is given by

$$G_{max} = \frac{d}{4}\left(\frac{f_d}{\Delta f}\right)^2 \tag{5.4}$$

where d is a correction factor with a typical value of 0.25 to account for the less than unity DC gain and the in-band gain reduction coming from the real pole and pair of complex zeros of the compensator. The achievable gain of 47dB at a 250Hz offset from 15kHz surpasses the open-loop gain requirement in the experimental prototype.

5.4 Positive Feedback Architecture

A practical positive feedback based $\Sigma\Delta$ architecture must be capable of forcing the open-loop DC gain below unity and must be tolerant of potential offsets in the sensor. In this section, we derive one such architecture.

5.4.1 Setting the Open-Loop DC Gain

Scaling the signal levels in the force feedback loop does nothing to the open-loop gain because the quantizer gain simply adjusts to keep it constant. Since, as mentioned previously, the quantizer gain is signal dependent, it is possible to force the DC gain below unity by injecting an appropriate amount of dither before the quantizer. Since the input variance of the quantizer increases while the output remains constant, the quantizer gain decreases, lowering with it the open-loop gain. A pseudo-random binary sequence is a good dither signal since it also helps to remove the tonal behavior of the modulator and is easily generated using a linear feedback shift register. The sequence does not degrade the overall interface noise floor since, like the quantization noise, it appears at the output frequency-shaped by both the sensor and the compensator. The dither signal can also be injected before the compensator, in which case it is important to inject dither that has undergone frequency-shaping to makeup for the loss of frequency shaping by the compensator. Figure 5.8 shows the alternative solutions. In the experimental prototype, the dither is injected before the compensator to reuse the DAC used to inject the calibration signal.

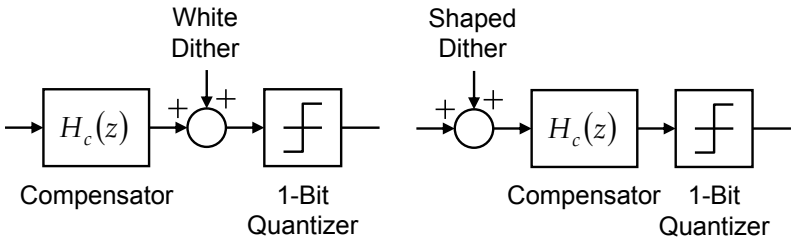

(a) (b)

Figure 5.8. Lowering quantizer gain by injecting (a) white dither before the quantizer, and (b) shaped dither before the compensator.

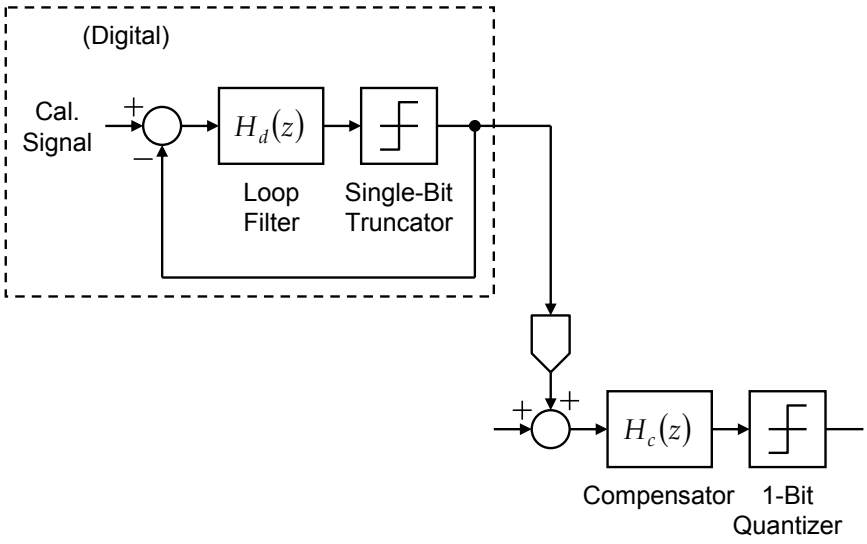

Figure 5.9. Using a digital $\Sigma\Delta$ modulator to reduce the analog complexity of the DAC, with the truncation noise doubling as dither.

In the interest of reducing analog complexity, the calibration signal can be band-pass $\Sigma\Delta$ modulated, then injected using a coarse DAC as shown in Figure 5.9 since the consequent truncation noise outside the desired signal band is acceptable. In fact, the truncation noise, having been shaped away from the desired signal band, can double as the dither, obviating the need for an additional frequency shaped dither. This, however, requires careful calibration of the coarse DAC gain to ensure that the truncation noise provides just the right amount of dithering. Because of the difficulty posed by MEMS and IC process tolerances, we avoid this solution in the experimental prototype and instead add a frequency shaped dither signal whose magnitude is digitally adjusted to the correct value, and reduce the truncation noise

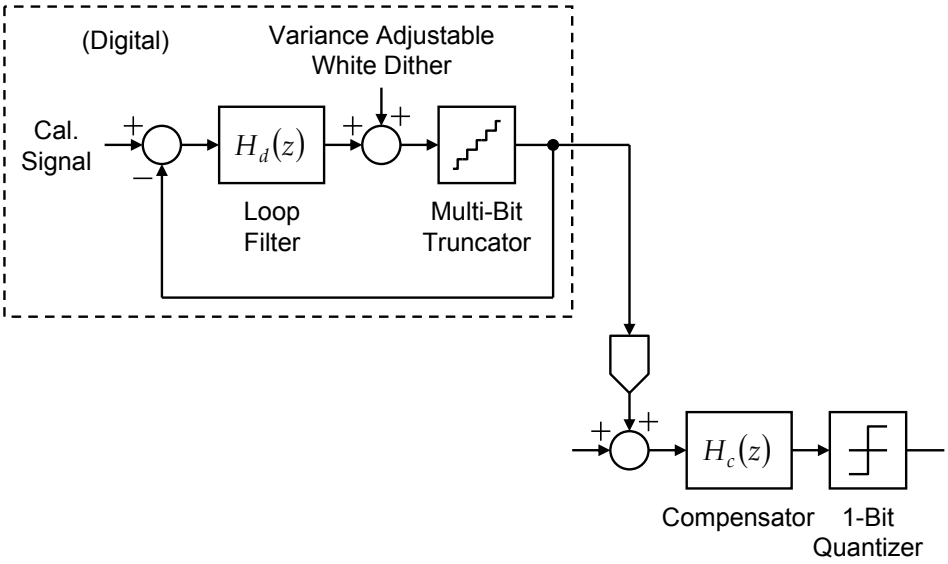

Figure 5.10. A more robust way to generate dither while minimizing analog complexity. The frequency shaped dither is realized by reusing the $\Sigma\Delta$ modulator to *Delta* modulate the variance adjustable white dither.

so that the process variation of the coarse DAC gain results in only a minor variation in the total dither. Figure 5.10 shows this solution. The frequency shaped dither is realized by reusing the $\Sigma\Delta$ modulator to Δ modulate a white dither signal whose variance is adjustable. Multi-bit truncation is necessary here to achieve the above mentioned truncation noise reduction.

The modulator requires, at minimum, a second-order band-pass loop filter to provide noise shaping equivalent to that provided by the compensator. An additional integrator, included to reject dither and truncation noise at low frequencies, prevents the injection of too much disturbance into the sensor at low frequencies where the force feedback loop gain is too low. The form of the loop filter is thus

$$H_d(z) = \underbrace{\frac{1}{z-1}}_{\substack{\text{low-}\\ \text{frequency}\\ \text{shaping}}} \underbrace{\frac{z^2 + d_1 z + d_2}{z^2 + cz + 1}}_{\substack{\text{in-band}\\ \text{shaping}}}. \tag{5.5}$$

where d_1 and d_2 control the pair of complex zeros that compensate the phase lag introduced by the pair of imaginary poles. The frequency of the pair of imaginary poles is controlled by c and therefore coincides with the frequency-shaping poles of the compensator. The loop filter is implemented entirely in the forward path with feed-forward summation to minimize the in-band input-to-output phase lag since

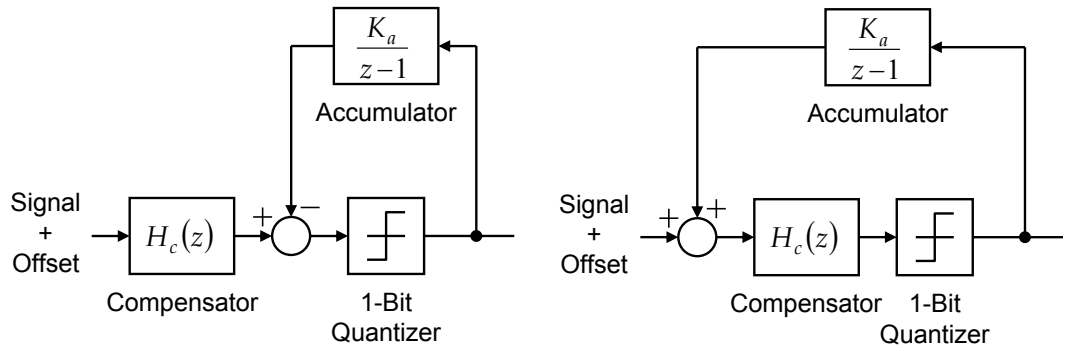

Figure 5.11. Accommodating sensor offset by applying offset compensation before (a) the quantizer, and (b) the compensator.

the mode-matching algorithm employs synchronous demodulation and is therefore sensitive to phase error.

5.4.2 Accommodating Sensor Offset

Due to fabrication tolerances and packaging stress, the sensor typically suffers from non-idealities such as non-zero nominal displacement from the balanced position and mismatch between the differential sense and parasitic capacitances. These non-idealities manifest as a DC or slowly drifting offset that often exceeds the full-scale measurement range of the sensor [14]. Having substantial loop gain at DC, traditional negative feedback loops easily accommodate the offset. The loss of feedback at DC in the positive feedback architecture results in the accumulation of offset before the quantizer, resulting in the departure of the quantizer gain from the desired value and consequent degraded operation. Fortunately, the problem is easily solved by a slow regulation loop that subtracts out the offset before the quantizer. Alternatively, the offset compensation signal can be applied before the compensator. In this case, the signal is added rather than subtracted since the compensator already performs sign inversion. Figure 5.11 shows the two possible solutions. Regulating the DC value of the output of the quantizer is permissible in this application since the Coriolis force is away from DC. We implement the second approach as shown in Figure 5.12 to reuse the already available system blocks. With this, we arrive at a system architecture that

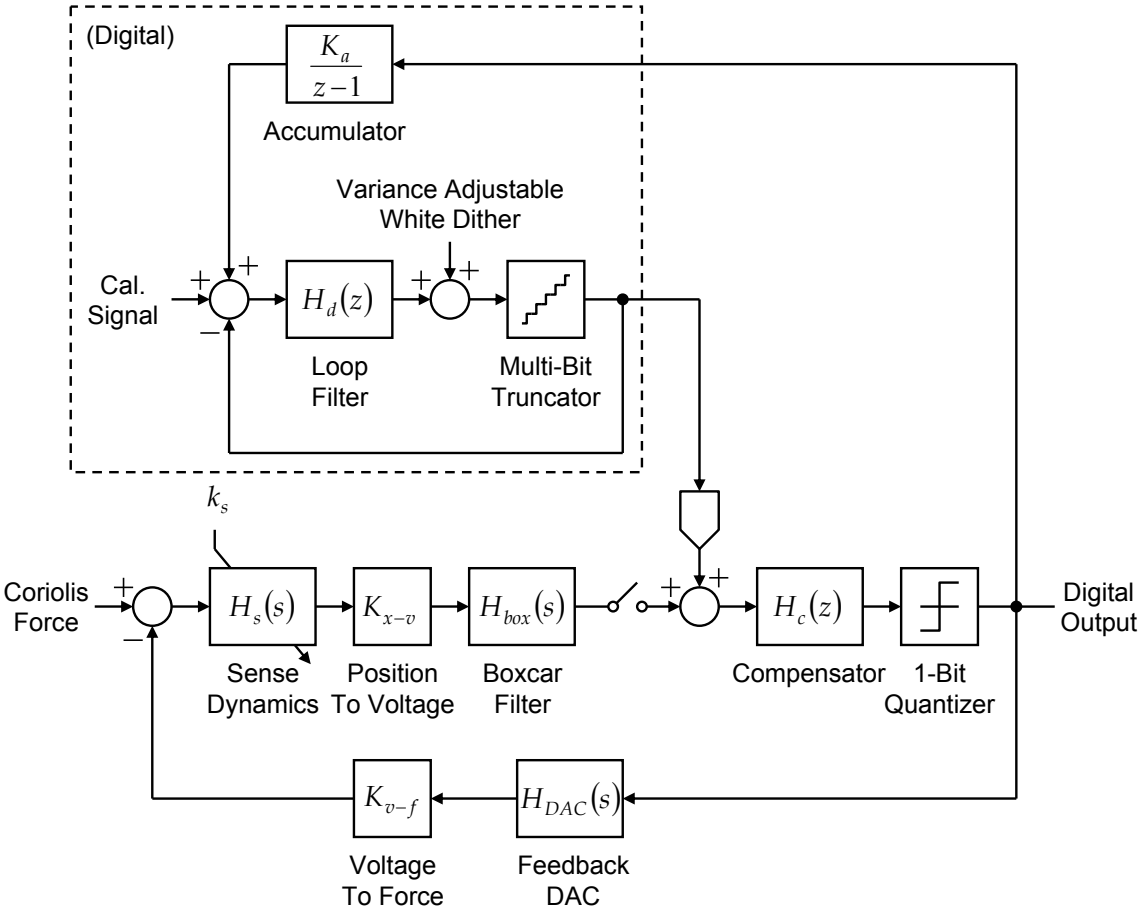

Figure 5.12. Final system architecture.

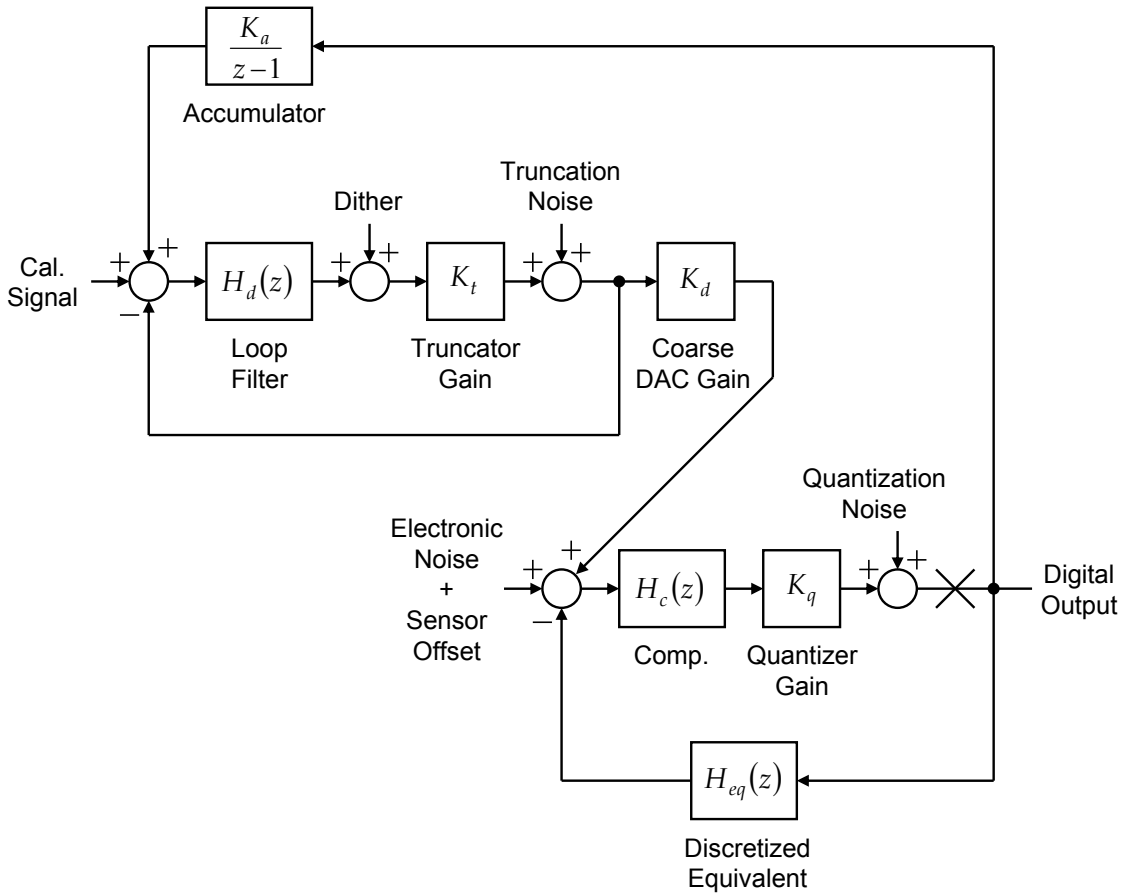

Figure 5.13. Analytical model of final architecture.

minimizes analog complexity while providing all the functions necessary for digital implementation of the mode-matching algorithm. Above all, the architecture is robust against parasitic resonances.

5.4.3 System Design

Figure 5.13 shows the analytical model for design. Arriving at a fully optimized design is quite challenging due to the nesting of the digital $\Sigma\Delta$ loop within the offset compensation loop, and interaction of the electronic loops with the main electromechanical loop. To make the process more tractable, we proceed incrementally starting with only the main electromechanical loop, adding the other loops as we proceed. The following is a design procedure that has been found to enable rapid specification of

all coefficients. Of course, the analytical results must always be verified and refined via simulation.

- Design the compensator to provide adequate phase margins for the discretized electromechanical chain with K_q adjusted to provide about 6dB of gain margin at DC. Over design of phase margin should be avoided since it requires the complex zeros and real pole of the compensator to move closer to the unit circle which penalizes the in-band gain.

- Design the digital $\Sigma\Delta$ modulator with the noise notches placed at both DC and the drive frequency. The white dither should be nominally sized to dominate over the truncation noise so that the process variation of the coarse DAC gain is easily accommodated by digitally resizing the white dither as mentioned previously. The number of truncation levels is as yet unimportant provided that it is enough to fully accommodate the truncation noise and dither.

- Close the offset compensation loop and choose the product of the accumulator and coarse DAC gains K_aK_d. The overall open-loop transfer function with the loop broken immediately after the quantizer (the spot marked by x in Figure 5.13) is

$$G_{open}(z) = K_qH_c(z)\left[H_{eq}(z) - \frac{\overbrace{K_aK_d}}{z-1}\frac{K_tH_d(z)}{1+K_tH_d(z)}\right]. \tag{5.6}$$

  Figure 5.14 shows how increasing values of K_aK_d affect the overall open-loop response. The offset compensation path introduces one more unity-gain point at low frequencies for a total of three unity-gain frequencies (with parasitic resonances excluded). This additional unity-gain frequency is critical since the phase also crosses over in that vicinity. Provided that doing so does not adversely impact phase margin, the product of the gains should be increased to maximize the bandwidth of the offset compensation loop to minimize the settling time during startup.

- While keeping the product K_aK_d constant, determine the value of K_d that provides just the right amount of dithering to force K_q to the value selected in the first step.

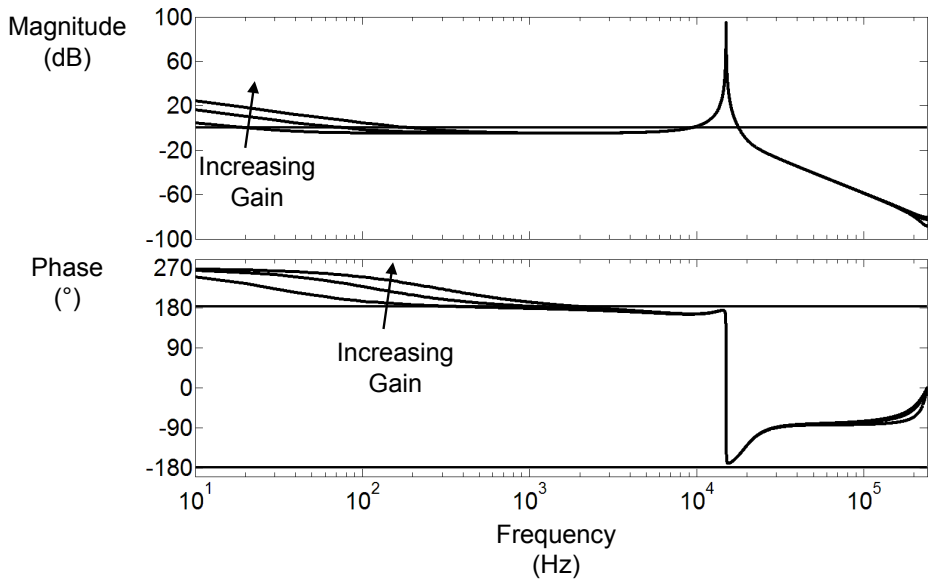

Figure 5.14. Effect of increasing the static gain of the offset compensation loop.

- Select the number of truncation levels that fully accommodates the calibration signal, the dither, and the worst case offset compensation signal.

The final step is verifying the overall system noise floor over the desired signal band taking into account electronic noise, quantization noise, truncation noise, and the dither. The transfer functions from the various noise inputs to the output are

$$NTF_q(z) = \frac{1}{1 + G_{open}(z)} \tag{5.7}$$

$$NTF_e(z) = \frac{K_q H_c(z)}{1 + G_{open}(z)} \tag{5.8}$$

$$NTF_t(z) = \frac{K_d}{1 + K_t H_d(z)} \frac{K_q H_c(z)}{1 + G_{open}(z)} \tag{5.9}$$

and

$$NTF_d(z) = \frac{K_d K_t}{1 + K_t H_d(z)} \frac{K_q H_c(z)}{1 + G_{open}(z)} \tag{5.10}$$

where $NTF_q(z)$ is for the quantization noise, $NTF_e(z)$ is for the electronic noise, $NTF_t(z)$ is for the truncation noise, and $NTF_d(z)$ is for the dither. Figure 5.15 shows the components of the output spectrum around the desired signal band for the experimental prototype and sensor obtained by the process outlined above. Truncation

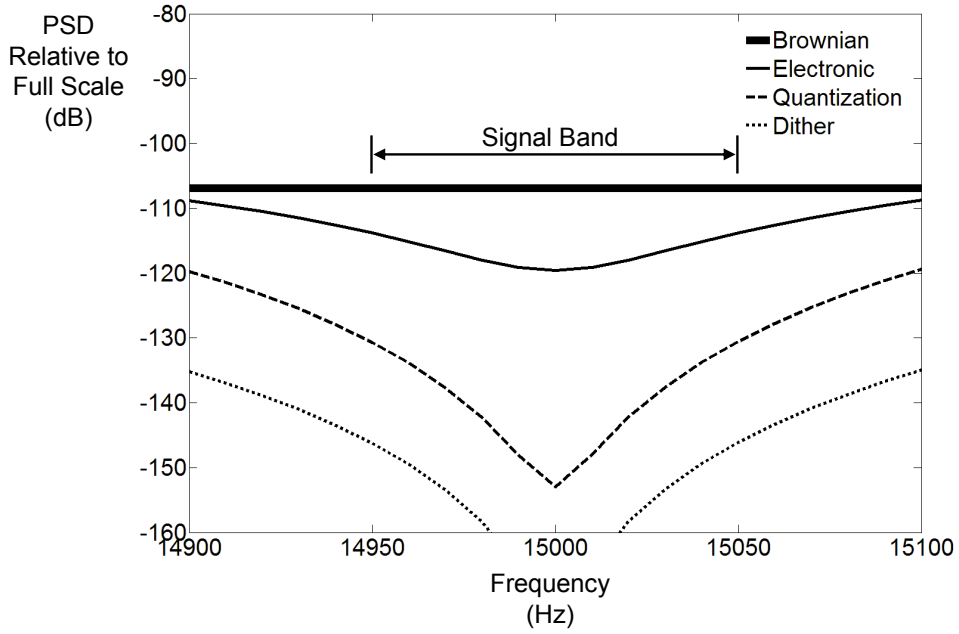

Figure 5.15. In-band output spectrum.

noise has been lumped together with the dither since they have the same shape. The intrinsic resolution of the front-end is preserved within the desired signal band since the electronic noise dominates over the other noise sources except for the Brownian noise, included for reference. The electronic noise is slightly over designed to prevent degradation of the overall SNR when small mode-matching errors exist.

5.5 Summary

In this chapter, bang-bang control is proposed as a way of avoiding the parasitic tuning of stiffness by the feedback voltage, and a positive feedback compensation technique is proposed as a way to overcome concerns of potential instability raised by the unavoidable parasitic resonances in practical vacuum packaged gyroscopes. From the positive feedback technique is developed a practical $\Sigma\Delta$ force feedback architecture that minimizes analog complexity by offloading a substantial amount of processing to the digital domain. Though relatively complex, the system is easy to design using a provided design procedure. In the next chapter, the techniques discussed here and in

previous chapters are applied towards the design of an experimental readout interface for a high-Q micromachined vibratory gyroscope.

Chapter 6

An Experimental Readout Interface

In this chapter, the techniques developed in the previous chapters are applied towards the implementation of an experimental readout interface in a 0.35μm CMOS process. The intended sensor has a drive resonance frequency of about 15kHz and a Brownian noise floor of about $0.004\,^\circ/\mathrm{s}/\sqrt{\mathrm{Hz}}$. The required bandwidth is 50Hz (100Hz double-sided). The operating frequency is locked to 32 times the sense element's drive resonance frequency of nominally 15kHz.

6.1 Implementation

Figure 6.1 shows the overall interface. The sense/feedback switch time-multiplexes the same set of electrodes between position sensing and feedback to implement collocated sensing and actuation. A digital estimator injects out-of-band pilot tones before the front-end to monitor the mismatch between the drive and sense resonance frequencies. The estimate feeds into an accumulator that generates a voltage used to electrostatically tune the sense resonance frequency. Eleven bit precision is needed to achieve the required tuning accuracy. The DAC is implemented with a 1-bit $\Sigma\Delta$ modulator followed by a switched-capacitor integrator that serves as the accumulator

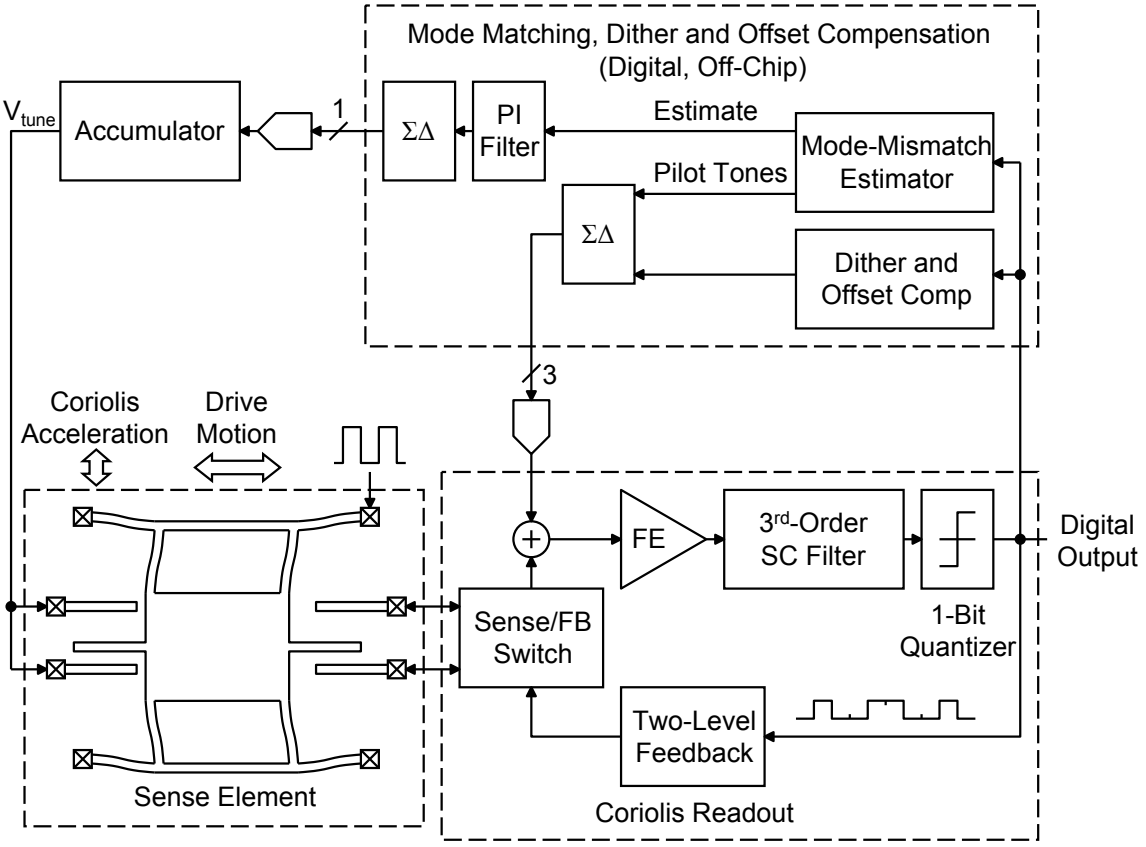

Figure 6.1. Interface block diagram.

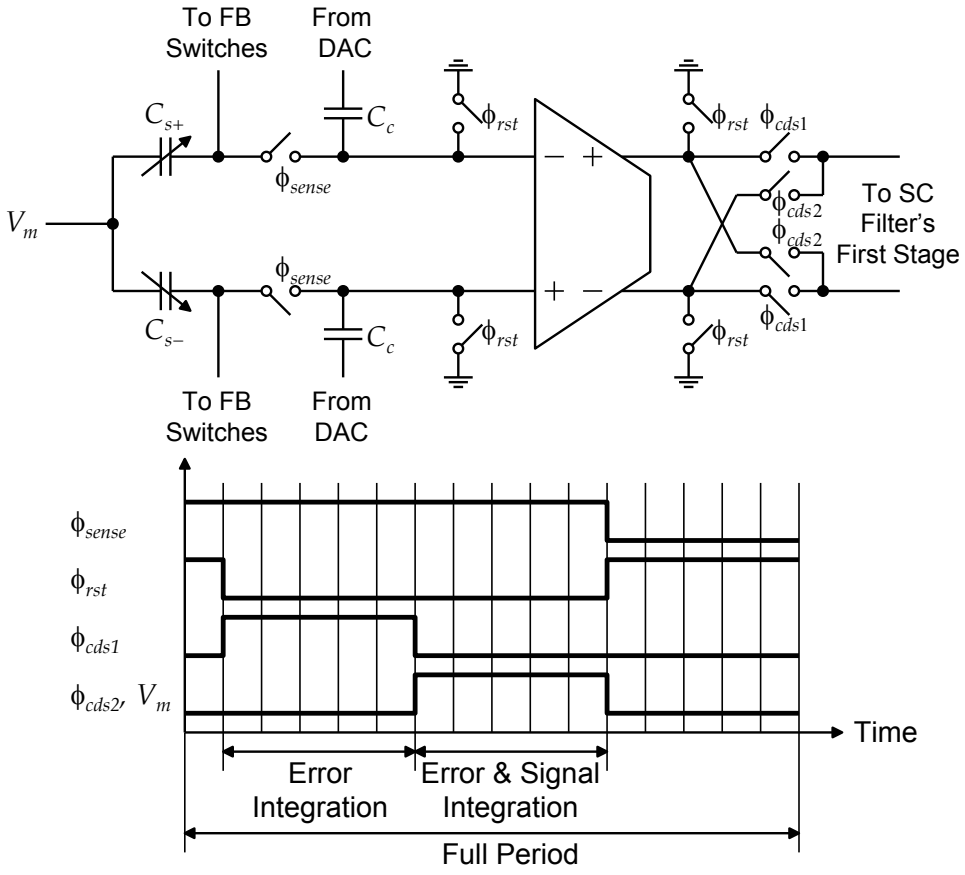

Figure 6.2. Schematic and timing of the front-end.

and doubles as reconstruction filter. Leak and offset in the integrator result in a systematic mode mismatch. A digital PI filter with infinite DC gain rejects this error. The modulated calibration, dither, and offset compensation signals are applied using a 3-bit DAC. By injecting them before rather than after the front-end amplifier, the large displacements are subtracted before the amplifier. The resulting smaller signal sensed by the front-end is advantageous for minimizing the adverse effects of jitter, drift, transconductance variation, and differential pair nonlinearity. The following subsections elaborate on the circuit details of key blocks.

6.1.1 Front-End and 3-Bit DAC

Figure 6.2 shows a schematic of the front-end with its timing diagram. The sense electrodes are connected to feedback voltages through feedback switches (omitted)

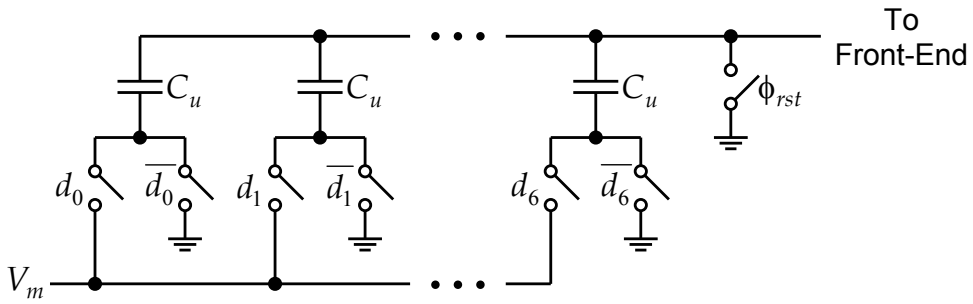

Figure 6.3. Simplified schematic of 3-bit DAC. Actual implementation is differential.

during the feedback phase and to the front-end amplifier through the sense switches during the sense phase. The output of the amplifier is connected directly to the following switched-capacitor filter through the CDS switches during the two integration phases and reset to ground when the front-end is inactive. The output of the 3-bit DAC is capacitively coupled to the input of the amplifier. The coupling capacitor is only 70fF, negligible compared to the 8pF of combined sense and parasitic capacitances.

Figure 6.3 shows the 3-bit DAC. It is shown as single-ended for simplicity, but the actual implementation is differential. It consists of seven unit elements that, depending on the input code, are connected to either ground or the proof mass node. When the pulse is applied on the proof mass, a voltage proportional to the capacitance imbalance between the sense capacitors, together with a voltage dependent on the input code of the DAC, develops at the input of the amplifier. The proof mass and DAC are excited by the same voltage pulse to keep the displacement to voltage gain and the DAC gain ratiometric.

Figure 6.4 shows the transistor-level circuit diagram of the front-end OTA. A folded cascode with PMOS inputs is chosen to enable an input common-mode level of V_{ss} (since the sense electrode are reset in preparation for position sensing). The double cascodes provide high output impedance.

6.1.2 Compensator

The first step in implementing the compensator is the synthesis of the transfer function out of only unit delay and gain elements. Figure 6.5 shows a realization that

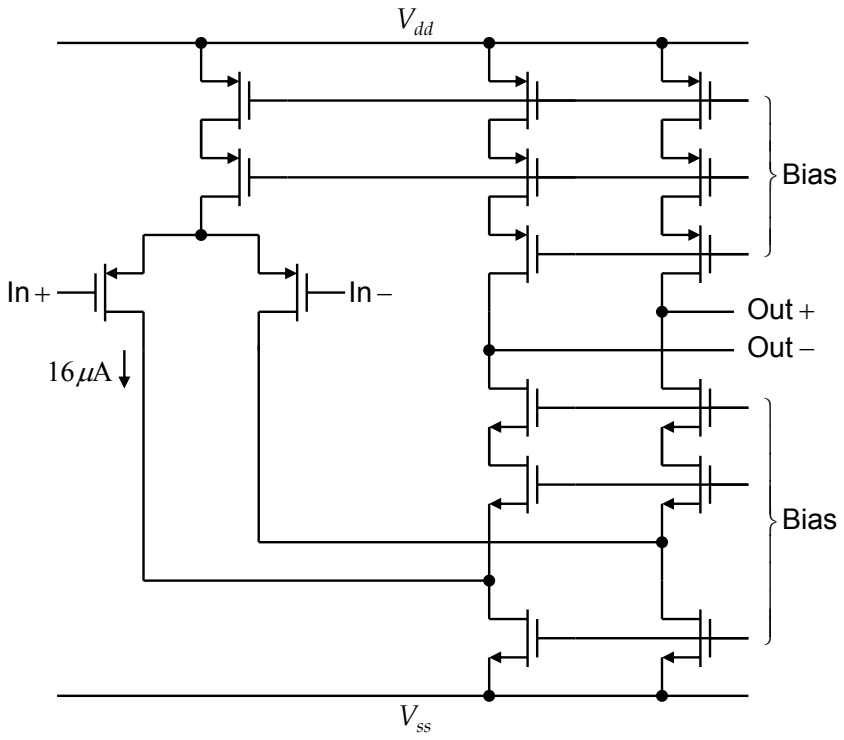

Figure 6.4. Front-end OTA schematic diagram.

places the delays strategically to minimize the settling path of the switched-capacitor integrator stages that ultimately implement the compensator. The resulting transfer function is

$$H_c(z) = -\frac{z}{z+a}\frac{z^2+b_1z+b_2}{z^2+cz+1} \tag{6.1}$$

where

$$a = k_1 - 1 \tag{6.2}$$

$$b_1 = k_2 + k_3 + k_4 - 2 \tag{6.3}$$

$$b_2 = 1 - k_3 \tag{6.4}$$

and

$$c = k_2 - 2. \tag{6.5}$$

The above system of equations can be solved to find the gains that yield the desired compensator coefficients. The gains should be rational to enable accurate realization

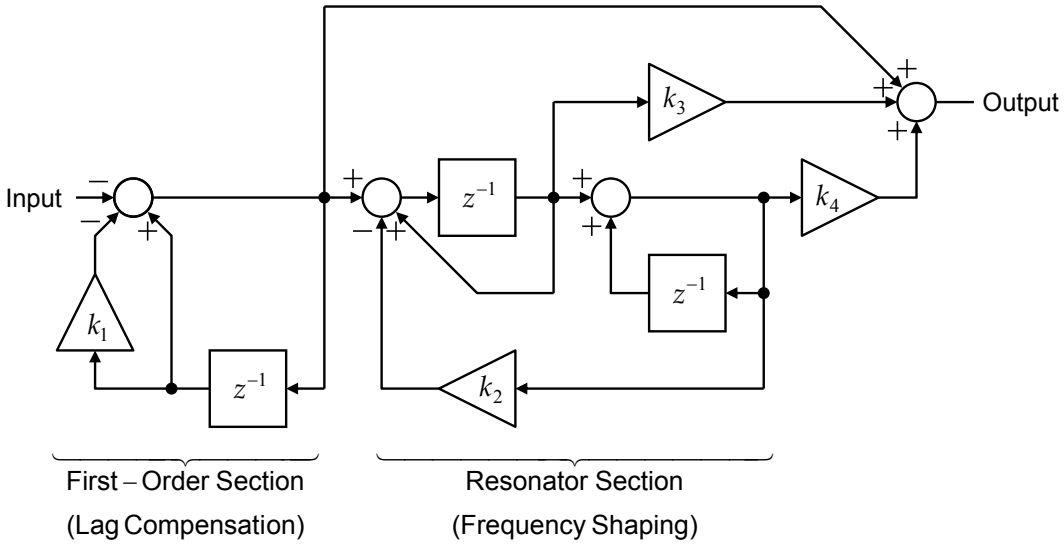

Figure 6.5. Synthesized compensator.

by simple capacitor ratios. This may require several iterations of the process of choosing the compensator coefficients so that, while meeting the other design goals, they also result in easily realizable gains.

Figure 6.6 shows the switched-capacitor circuit implementation of the compensator. Final summation of the signals from the resonator and the feed forward paths is realized passively to avoid additional power dissipation. The gain error introduced by the parasitic capacitances at the summation node is unproblematic since the comparator following the filter is sensitive only to the polarity of the signal. Input sampling capacitors are absent since the output current of the front-end during the two correlated double sampling phases integrates directly onto the integration capacitors of the first stage. The extra time during which the front-end is inactive allows the amplifier stages to settle and the comparator to reach a bit decision. This extra time is the source of the processing delay mentioned in the previous chapter. The amplifiers are one fifth scale versions of the fully differential folded double cascode OTA used in the front-end. The capacitor ratios are related to the gains above as follows:

$$k_1 = \frac{C_{f1}}{C_{I1}} \tag{6.6}$$

$$k_2 = \frac{C_{f2}}{C_{I2}} \frac{C_{s2}}{C_{I3}} \tag{6.7}$$

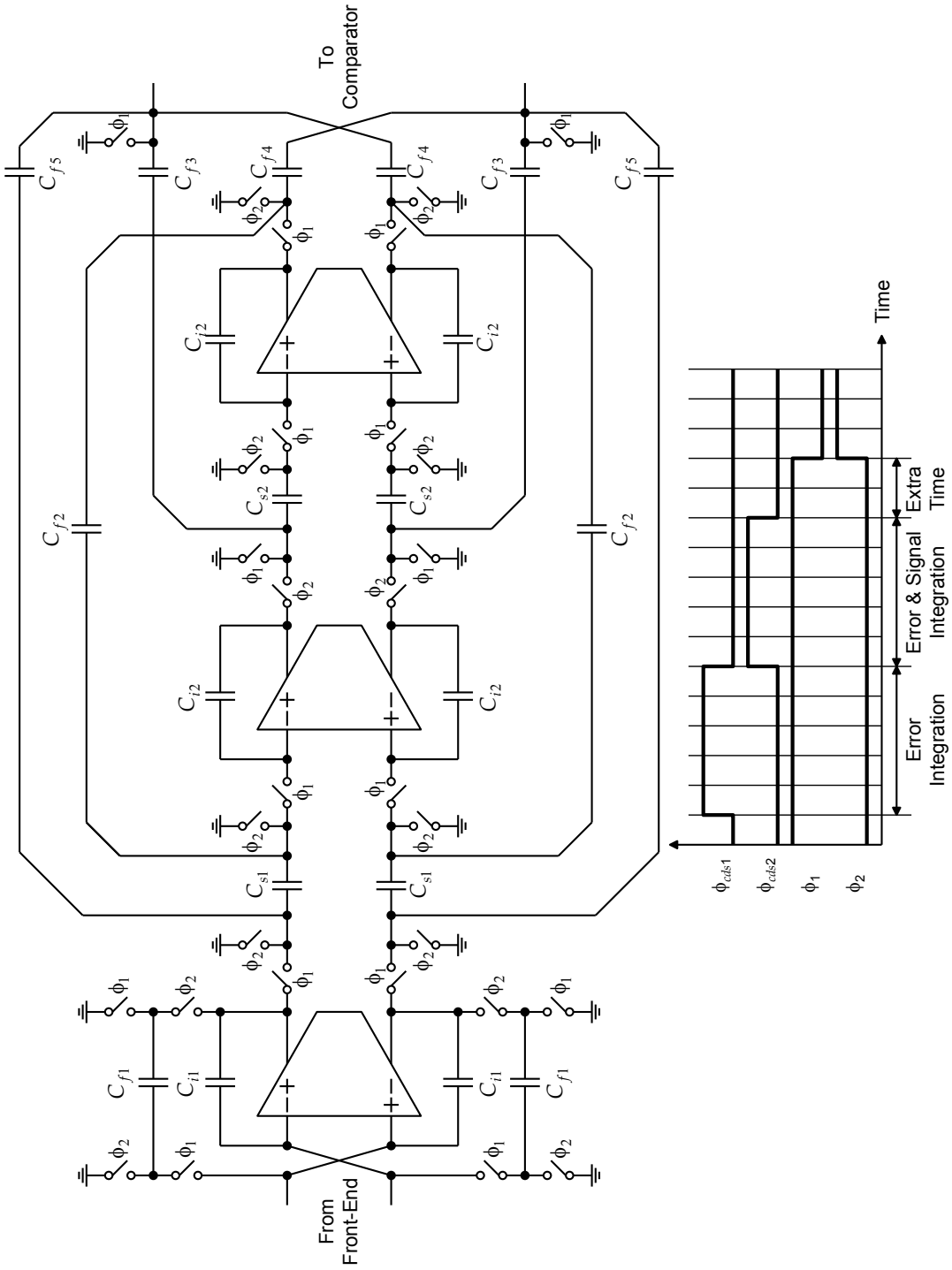

Figure 6.6. Switched-capacitor circuit implementation of the compensator.

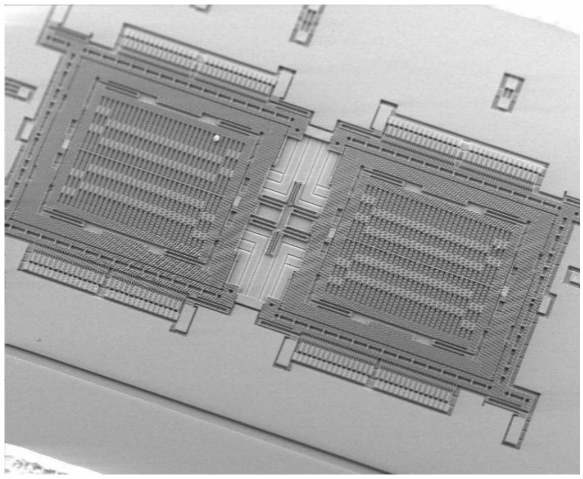

Figure 6.7. SEM of the sense element. The sense element consists of two mechanically coupled sensing structures.

$$k_3 = \frac{C_{s1}}{C_{I2}} \frac{C_{f3}}{C_{f5}} \tag{6.8}$$

$$k_4 = \frac{C_{s1}}{C_{I2}} \frac{C_{s2}}{C_{I3}} \frac{C_{f4}}{C_{f5}} \tag{6.9}$$

The gain of the front-end depends on the front-end OTA transconductance, the integration time, and the load capacitor which, in this case, is C_{I1}. C_{I1} is chosen large enough to keep the signal swing within the supply. In this design, $G_m = 160$uS, $T_{int} = 0.65$us, and $C_{I1} = 1$pF, resulting in a front-end gain of about 40dB. This gain is large enough that the noise of the filter is negligible but is not too large that the OTA and sensor offsets exceed the output swing of the first integrator. The values of the rest of the capacitors are chosen as a tradeoff between matching, and power consumption while satisfying the ratios above.

6.2 Experimental Results

The interface was designed and fabricated in a 0.35μm CMOS process and tested with the gyroscope presented in [26]. Figure 6.7 shows an SEM of the sense element. Figure 6.8 shows the measured frequency response of the sense axis. Besides the main resonance near 15kHz, many parasitic resonance modes can be found across a wide

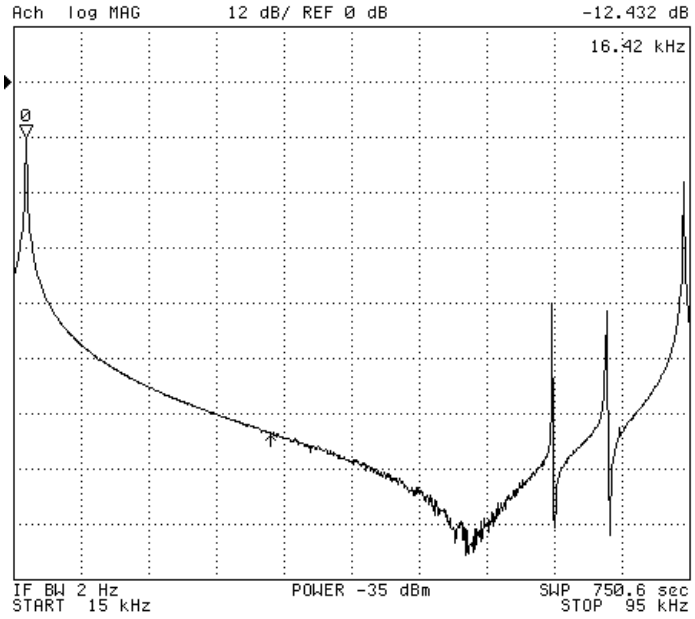

(a)

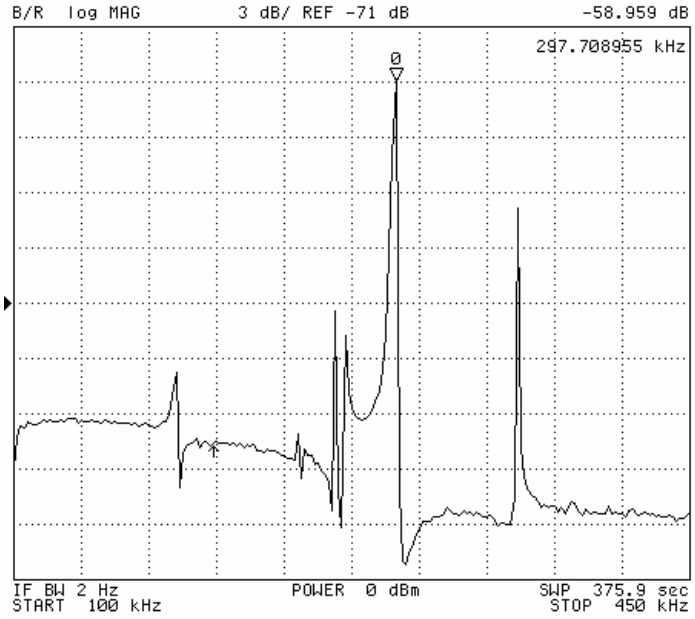

(b)

Figure 6.8. Measured frequency response of the sense axis. (a) From 15kHz to 95kHz. (b) From 100kHz to 450kHz

.

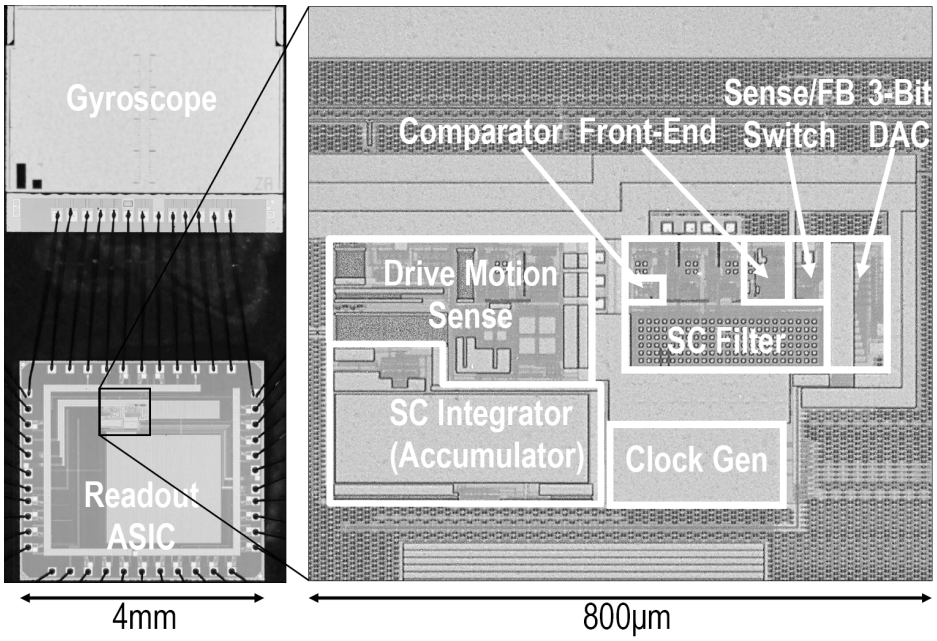

Figure 6.9. Die photo of interface.

frequency range, the major ones being around 95kHz and 300kHz. These modes, normally problematic for loops employing traditional lead compensation, are easily accommodated by the positive feedback compensation scheme.

Figure 6.9 shows a micrograph of the packaged sense element and readout ASIC. The interface occupies an active area of $0.8 \times 0.4\text{mm}^2$ and consumes less than 1mW from 3.3V and 12V. The 12V is used by the high-voltage switched-capacitor integrator (accumulator) that generates the electrostatic tuning voltage. Approximately 20% of the power is dissipated in the position sense front-end and 10% is dissipated in the switched-capacitor filter. Another 10% is dissipated in the high-voltage switched-capacitor integrator, and about 40% is due to CV^2 losses incurred in switching the proof mass and sense nodes of the sense element during the various phases of each sampling period. Additional circuits (not included in the 1mW) are a conventional switched-capacitor charge integrator front-end and buffers to detect the drive motion of the gyroscope. The digital blocks, including the digital $\Sigma\Delta$ modulators, the digital PI filter, and the calibration signal synthesizer and demodulator, were implemented in a Xilinx FPGA. The packaged gyroscope and readout ASIC were mounted on a test board that includes regulators to provide stable supply voltages, potentiometers

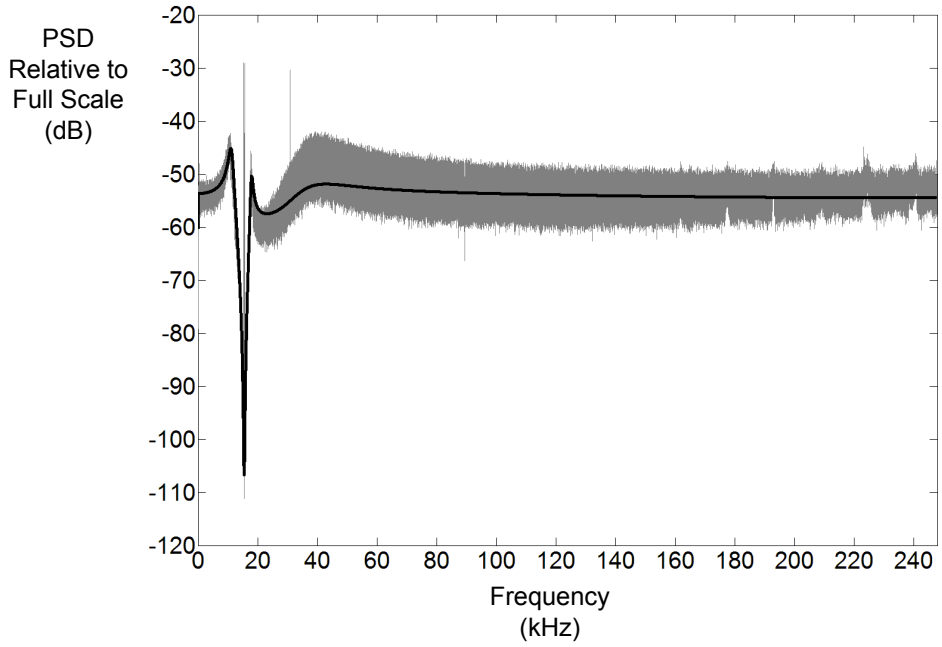

Figure 6.10. Measured output spectrum. The solid dark line is the analytically predicted output spectrum.

for bias current generation, and buffers for driving the FPGA. The test board was mounted on a rate table to perform angular rate measurements.

Figure 6.10 compares the measured output spectrum to the analytically predicted output spectrum. The overall shape of the output spectrum is in good agreement with the prediction of the describing function model. Figure 6.11 shows the output spectrum measured with and without calibration in the presence of an angular rate sinusoidally varying at 25Hz with an amplitude of 5.3°/s. The sinusoidal rate signal appears amplitude modulated at the drive frequency of 15.49kHz. The spectral component coincident with the drive frequency is due to Coriolis offset and quadrature error. The spectral components at about 250Hz offset from the drive frequency are the pilot tones. Calibration prevents the misplacement of the noise notch inherent in the uncalibrated system. The in-band portion of the output spectrum indicates a reduction of the noise floor from $0.04\,^{\circ}/\mathrm{s}/\sqrt{\mathrm{Hz}}$ to $0.004\,^{\circ}/\mathrm{s}/\sqrt{\mathrm{Hz}}$.

Figure 6.12 shows the measured electrostatic tuning voltage during startup. The calibration loop settles within 80ms.

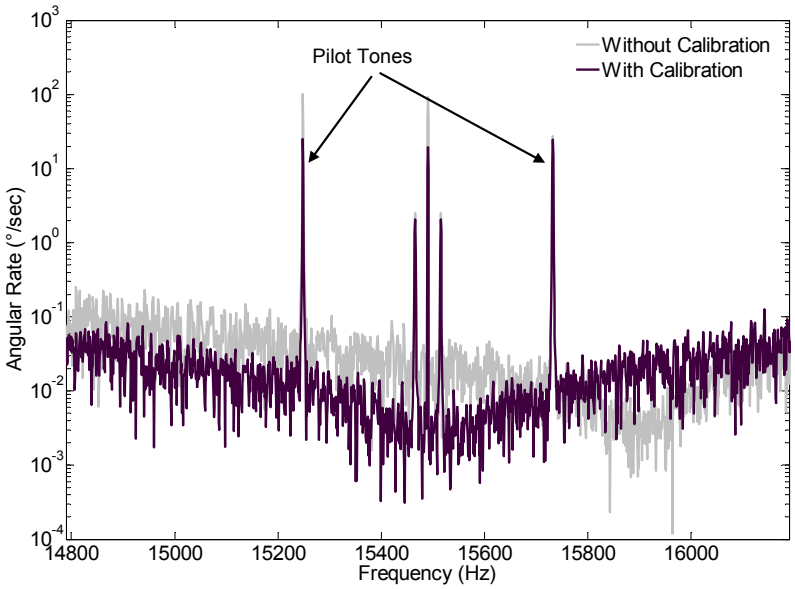

(a)

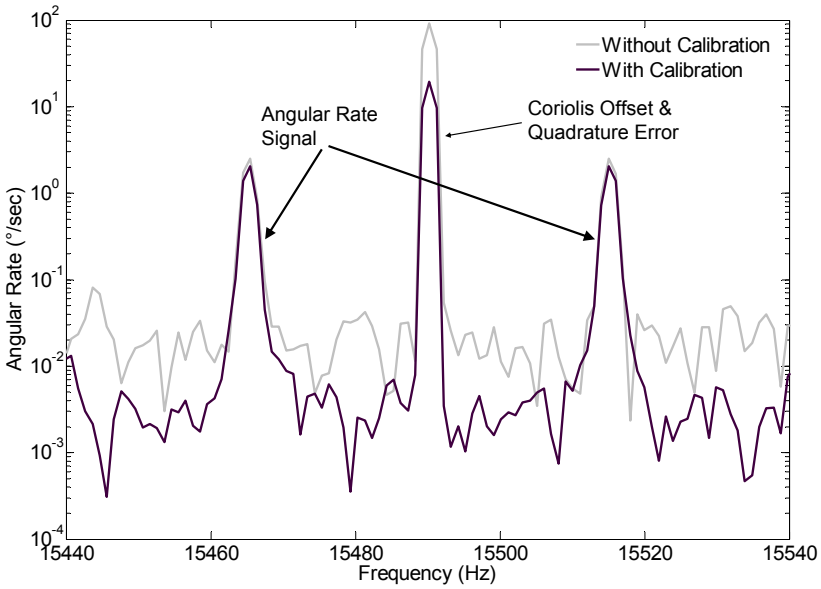

(b)

Figure 6.11. Measured output spectrum showing (a) the misplaced noise notch in the uncalibrated system, and (b) the improvement in the in-band noise floor with calibration

.

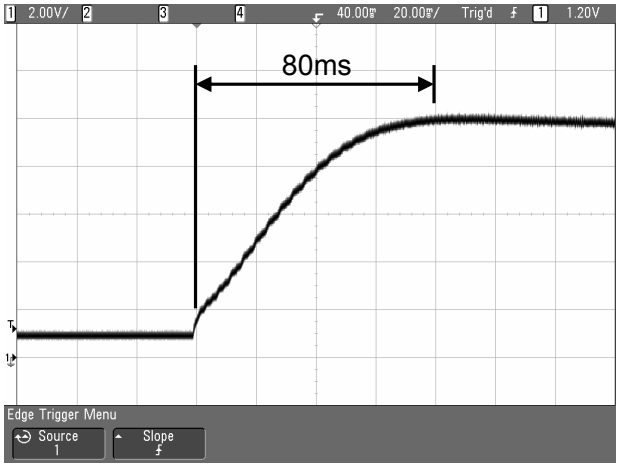

Figure 6.12. Tune voltage during startup.

6.3 Summary

The techniques covered in the previous chapters have been implemented and verified by measurement. The mode-matching algorithm calibrates the sense resonance frequency to match the drive frequency. The resulting increased mechanical amplification results in improved SNR. The boxcar sampling used within a force feedback loop improves front-end power efficiency without introducing errors. The positive feedback compensation scheme accommodates high-Q parasitic resonance modes of the sense element. Measurement results with the particular sense element indicate that the noise floor within the desired signal band is dominated by Brownian noise.

Chapter 7

Conclusions

7.1 Results

Matching the drive and sense resonance frequencies of a vibratory gyroscope enables substantial improvements in the power efficiency of the readout interface, but implies certain architectural choices. This dissertation presents the architecture and circuits used to exploit the sense resonance to achieve more than 30dB improvement in the Coriolis acceleration noise floor over traditional solutions dissipating the same amount of power. 20dB of the power savings comes from the mechanical amplification provided by the sense resonance. The remaining 10dB comes from the use of boxcar sampling.

The system architecture developed here uses background calibration to match the drive and sense resonance frequencies beyond fabrication tolerances to enable the full exploitation of the sense resonance. It uses force feedback to overcome challenges such as limited sense bandwidth and poor scale factor stability brought about by mode-matching. It uses bang-bang control to prevent the feedback voltage from inadvertently tuning the sense resonance, and uses a positive feedback compensation technique to ensure that the force feedback loop remains stable and robust against the parasitic resonance modes of the sense element. The ultimate result is the first

experimentally verified 1mW gyroscope readout interface with a $0.004\,^{\circ}/\mathrm{s}/\sqrt{\mathrm{Hz}}$ noise floor over a 50Hz band.

7.2 Future Work

With the several order-orders-of-magnitude improvement in the readout interface power efficiency, the impact of the drive circuit power dissipation gains in significance. Research into low-power drive circuits is therefore a logical next step. Besides power dissipation, other important metrics for the drive circuit are the temperature stability of the drive amplitude and the time from startup to steady-state oscillation. Temperature stability is especially critical in inertial navigation applications where the variation of the scale factor in the presence of a Coriolis offset can appear as a large bias drift. The time from startup to steady-state oscillation is important in image stabilization applications where the gyroscope is usually only briefly activated when a picture is being taken. Achieving good temperature stability and fast startup at much lower power than is used presently is one of the major challenges for future research.

Bibliography

[1] W. A. Clark, *Micromachined Vibratory Rate Gyroscopes*. PhD thesis, Electrical Engineering and Computer Sciences, University of California, Berkeley, 1997.

[2] J. A. Geen, S. J. Sherman, J. F. Chang, and S. R. Lewis, "Single-chip surface micromachined integrated gyroscope with 50°/h Allan deviation," *IEEE Journal of Solid-State Circuits*, vol. 37, pp. 1860–1866, Dec. 2002.

[3] W. A. Clark, R. T. Howe, and R. Horowitz, "Surface micromachined Z-axis vibratory rate gyroscope," in *Technical Digest of the Solid-State Sensor and Actuator Workshop*, (Hilton Head Island, SC), pp. 283–287, 1996.

[4] M. S. Weinberg and A. Kourepenis, "Error sources in in-plane silicon tuning-fork MEMS gyroscopes," *Journal of Microelectromechanical Systems*, vol. 15, pp. 479–491, June 2006.

[5] M. W. Putty and K. Najafi, "A micromachined vibrating ring gyroscope," in *Technical Digest of the Solid-State Sensor and Actuator Workshop*, (Hilton Head Island, SC), pp. 213–220, 1994.

[6] J. Choi, K. Minami, and M. Esashi, "Silicon resonant angular rate sensor by reactive ion etching," in *Technical Digest of the 13th Sensor Symposium*, (Tokyo, Japan), pp. 177–180, 1995.

[7] W. Yun, R. T. Howe, and P. R. Gray, "Surface micromachined, digitally force-balanced accelerometer with integrated CMOS detection circuitry," in *Technical Digest of the Solid-State Sensor and Actuator Workshop*, (Hilton Head Island, SC), pp. 126–131, 1992.

[8] Analog Devices, One Technology Way, Norwood, MA 02062, *ADXL50: Monolithic accelerometer with signal conditioning*.

[9] A. Sharma, M. Zaman, and F. Ayazi, "A 0.2°/hr mirco-gyroscope with automatic CMOS mode matching," in *ISSCC Digest of Technical Papers*, (San Fransisco, CA), pp. 386–387, 2007.

[10] X. Jiang, *Capacitive Position-Sensing Interface for Micromachined Inertial Sensors*. PhD thesis, Electrical Engineering and Computer Sciences, University of California, Berkeley, 2003.

[11] V. P. Petkov, *High-Order ΣΔ Interface for Micromachined Inertial Sensors*. PhD thesis, Electrical Engineering and Computer Sciences, University of California, Berkeley, 2004.

[12] J. I. Seeger, X. Jiang, M. Kraft, and B. E. Boser, "Sense finger dynamics in a ΣΔ force-feedback gyroscope," in *Technical Digest of the Solid-State Sensor and Actuator Workshop*, (Hilton Head Island, SC), pp. 296–299, 2000.

[13] A. Preumont, *Vibration Control of Active Structures: An Introduction*. Kluwer Academic Publishers, 2nd ed., 2002.

[14] M. Lemkin and B. E. Boser, "A three-axis micromachined accelerometer with a CMOS position-sense interface and digital offset-trim electronics," *IEEE Journal of Solid-State Circuits*, vol. 34, pp. 456–468, Apr. 1999.

[15] J. Wu, G. K. Fedder, and L. R. Carley, "A low-noise low-offset capacitive sensing amplifier for a 50-$\mu g/\sqrt{\text{Hz}}$ monolithic CMOS MEMS accelerometer," *IEEE Journal of Solid-State Circuits*, vol. 39, pp. 722–730, May 2004.

[16] C. C. Enz and G. C. Temes, "Circuit techniques for reducing the effects of op-amp imperfections: autozeroing, correlated double sampling, and chopper stabilization," *Proceedings of the IEEE*, vol. 84, pp. 1584–1614, Nov. 1996.

[17] M. Lemkin, *Micro Accelerometer Design with Digital Feedback Control*. PhD thesis, Electrical Engineering and Computer Sciences, University of California, Berkeley, 1997.

[18] C. Lang and R. Tielert, "A low noise accelerometer with digital PID-type controller and multibit force feedback," in *Proceedings of the 25th European Solid-State Circuits Conference*, (Neuily sur Seine, France), pp. 250–253, 1999.

[19] T. Smith, O. Nys, M. Chevroulet, Y. DeCoulon, and M. Degrauwe, "A 15b electromechanical sigma-delta converter for acceleration measurements," in *ISSCC Digest of Technical Papers*, (San Fransisco, CA), pp. 160–161, 1994.

[20] X. Jiang, J. I. Seeger, M. Kraft, and B. E. Boser, "A monolithic surface micromachined Z-axis gyroscope with digital output," in *Symposium on VLSI Circuits Digest of Technical Papers*, (Honolulu, HI), pp. 16–19, 2000.

[21] H. Kulah, A. Salian, N. Yazdi, and K. Najafi, "A 5V closed-loop second-order sigma-delta micro-g micro accelerometer," in *Technical Digest of the Solid-State Sensor and Actuator Workshop*, (Hilton Head Island, SC), pp. 219–222, 2002.

[22] V. P. Petkov and B. E. Boser, "A fourth-order ΣΔ interface for micromachined inertial sensors," *IEEE Journal of Solid-State Circuits*, vol. 40, pp. 1602–1609, Aug. August 2005.

[23] H. Kulah, J. Chae, N. Yazdi, and K. Najafi, "Noise analysis and characterization of a sigma-delta capacitive microaccelerometer," *IEEE Journal of Solid-State Circuits*, vol. 41, pp. 352–361, Feb. 2006.

[24] J.-J. E. Slotine and W. Li, *Applied Nonlinear Control*. Prentice Hall, 1991.

[25] S. R. Norsworthy, R. Schreier, and G. C. Temes, eds., *Delta-Sigma Data Converters: Theory, Design, and Simulation*. IEEE Press, 1997.

[26] U.-M. Gómez, B. Kuhlmann, J. Classen, W. Bauer, C. Lang, M. Veith, E. Esch, J. Frey, F. Grabmaier, K. Offterdinger, T. Raab, H.-J. Faisst, R. Willig, and R. Neul, "New surface micromachined angular rate sensor for vehicle stabilizing systems in automotive applications," in *Proceedings of the 13th International Conference on Solid State Sensors, Actuators and Microsystems*, (Seoul, Korea), pp. 184–187, 2005.